

NASA Technical Memorandum 85636 NASA-TM-85636 19830020713

PROPELLER NOISE PREDICTION

William E. Zorumski

May 1983

LIBRARY COPY

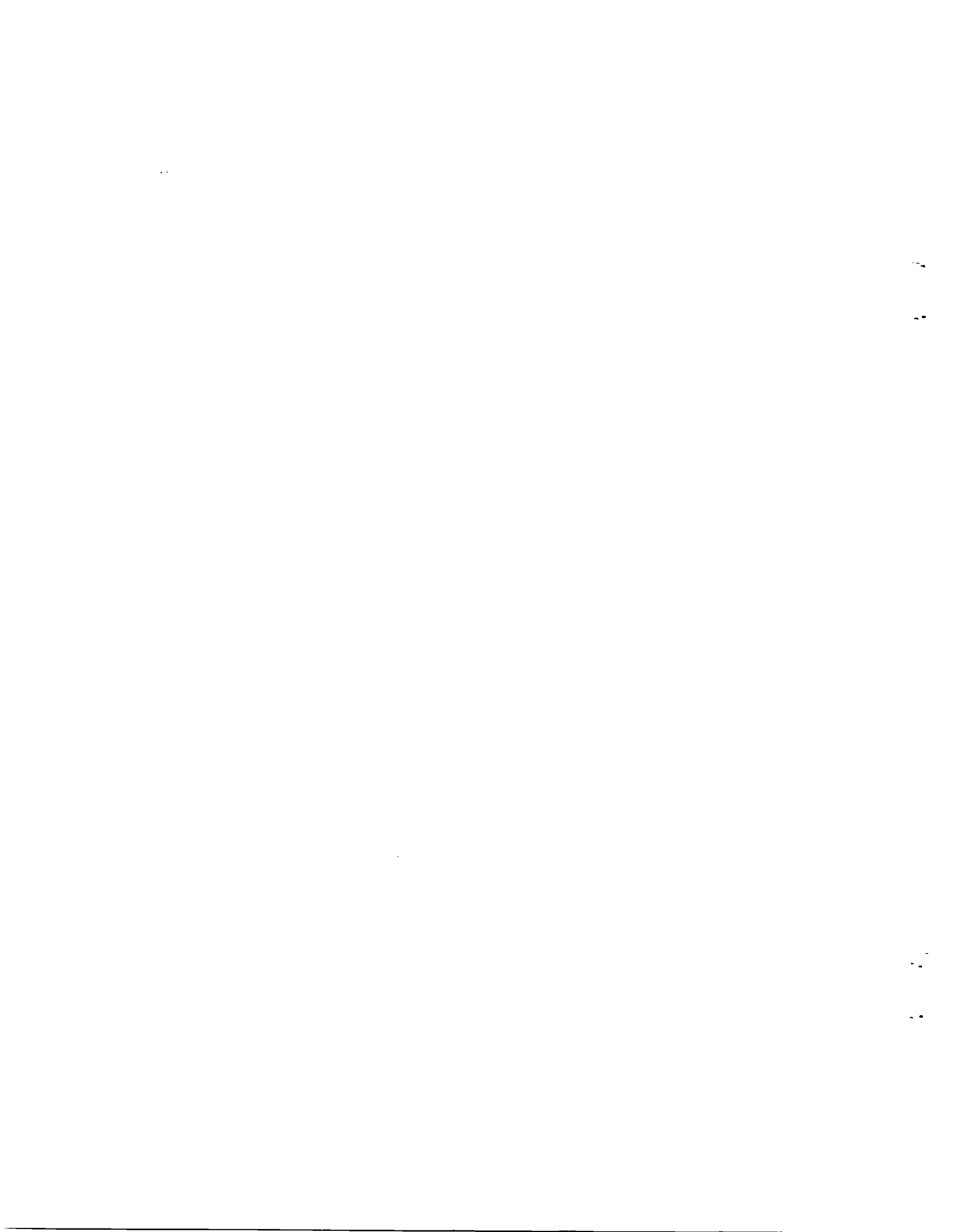
JUN 23 1983

LANGLEY RESEARCH CENTER
LIBRARY, NASA
HAMPTON, VIRGINIA



National Aeronautics and
Space Administration

Langley Research Center
Hampton, Virginia 23665



SUMMARY

3 1176 01323 7996

The NASA Aircraft Noise Prediction Program (ANOPP) Propeller Analysis System is a set of computational modules for predicting the aerodynamics, performance, and noise of propellers. Propeller blade geometry is given in terms of blade surface coordinates derived from a Joukowski transform of the blade sections. Potential flow around the blade sections is computed by Theodorsen's method using the Kutta condition to fix the circulation. Blade boundary layers are computed using the Holstein-Bohlen method in the laminar region and the Truckenbrodt method in the turbulent region. Profile drag is predicted by the method of Young and Squires. Performance and induced flow are computed by Lock's method with the Prandtl circulation function near the blade tip. Discrete tone noise is predicted from blade shape and aerodynamic loads using Farassat's methods: the blade surface integral method for subsonic propellers and the collapsing sphere method for transonic propellers. Broadband trailing edge noise is computed by Schlinker and Amiet's method. The results of this prediction system are compared to measurements on two propellers: one subsonic and one transonic. Nearfield levels on the subsonic propeller are accurately predicted if the predicted power coefficient is adjusted to match the measured power coefficient of the propeller. The lower frequency harmonics of the subsonic propeller spectrum match the measured values but the high frequency harmonics are underpredicted. This underprediction is believed to be due to the omission of unsteady loading effects in the predictions. The farfield or flyover noise of the subsonic propeller is scattered by atmospheric and ground effects but the general trend of the data indicates overprediction of farfield levels. Transonic propeller noise measured on the fuselage of the aircraft is

N 83-28984 #

significantly influenced by the refraction effects of the boundary layer on the fuselage. When these effects are included and when the power is matched, the transonic predictions agree with the data except in a small region just behind the propeller plane on the aircraft surface. It is believed that scattering effects may be the cause of this discrepancy.

INTRODUCTION

Propeller noise prediction is based on two disciplines: aerodynamics and acoustics. NASA has developed a computer system for propeller noise prediction using the assumption that these disciplines are separable, that is, that the flow field can be separated into an aerodynamic part and an acoustic part. This separation allows the computations to be made sequentially. Classical aerodynamic theory is used to find the surface pressures and frictional stresses on the blade surfaces and then acoustic theories are used to predict the noise.

The prediction system is diagrammed in figure 1. The different computational tasks are assigned to independent blocks of computer code called functional modules. These modules are managed by an executive system, the ANOPP executive program (reference 1). One group of modules deals with the aerodynamic computations. Not shown are modules which compute atmospheric properties and flight dynamics. These modules are described in reference 2. The end products of the aerodynamics modules are the propeller blade motions and loads. Motions include only the aircraft motion and rotational effects. Flexing and vibration, while possibly important, are not included at this time. The loads are the pressure and frictional stress on the propeller blade surface. These loads are generally a function of both surface position and time. Given the blade motions and loads, it is theoretically possible to predict the noise. As a practical matter, however, this prediction is impossible. The loads are really non-stationary random processes and there is presently no feasible computational procedure which will produce a complete description of the noise. The approximation is made that the noise may be divided into two parts: discrete and broadband. The discrete tone noise is

computed directly from the blade motions and loads while the broadband noise is estimated by semi-empirical methods. The tone noise computations are made entirely with time domain techniques while broadband noise estimates use a blend of frequency and time domain concepts.

Noise predictions are needed in both the near and far field. Nearfield noise predictions are needed to find the noise transmitted to the interior of an aircraft. There are two important nearfield effects on propeller-generated noise. These effects are the refraction caused by nonuniform flow over the aircraft and the scattering by the aircraft body. Farfield effects are needed to accurately predict community noise. These effects are the atmospheric attenuation and refraction, and the ground effects of reflection and absorption. Further information on the farfield propagation modules may be found in reference 2. Modules for the nearfield effects will be described in more detail here.

Agreement with experiment is the ultimate goal of a prediction system. Any prediction method, a guess, a curve fit, or a solution to a partial differential equation, is acceptable if it agrees with experimental data according to some objective rule. The question is how many experiments and how good must the agreement be to prove that a prediction is correct. This question raises the second question: prove it to whom? You cannot prove to a member of the Flat Earth Society that the earth is round.

Despite these minor difficulties, we gather data from experiments in the hope of proving that the prediction system is correct. These are indicated in figure 1 as flight data and tunnel data to denote the two types of facilities most frequently used to conduct the experiments. The flight data are usually but not always full scale. Results will be shown later for two propellers:

one subsonic design and one transonic design. The subsonic propeller is made by the Hartzell Company and its noise was measured by a wing-mounted boom microphone in flight. The transonic propeller is the NASA SR-3 Propfan design. This roughly quarter-scale propeller was tested in flight mounted atop a Jetstar aircraft.

SYMBOLS

a	radius of perfect circle
b	Joukowski transform parameter
C	blade section chord
C_d	blade section drag coefficient re section dynamic pressure and chord
C_D	energy dissipation coefficient
C_f	skin friction coefficient re section dynamic pressure
C_ℓ	blade section lift coefficient re section dynamic pressure and chord
C_n	Theodorsen transform coefficients
C_p	coefficient of pressure re section dynamic pressure
C_T	wall shear stress coefficient re local dynamic pressure
c_∞	ambient speed of sound
F	Prandtl tip vorticity function
H_{ij}	boundary layer shape factors, $i \neq j = 1, 2, 3$
$H_m^{(1)}, H_m^{(2)}$	Hankel functions of the first and second kinds
i	unit imaginary number
J	advance ratio V_∞/nD
k_x, k_y, k_r	wave numbers
$\vec{\ell}$	loading intensity vector
ℓ_y	empirical broadband correlation length
M_h	tip helical Mach number
M_r	radiation Mach number

M_t	tip rotational Mach number
M_∞	freestream or forward Mach number
m	circumferential harmonic number
M	blade section Mach number
\vec{n}	normal to blade surface
p	acoustic pressure
r, θ, z	cylindrical coordinates
R	propeller disk radius
\vec{r}	radiation vector $\vec{x}-\vec{y}$
\hat{r}	unit radiation vector
S	surface area
$S(\omega)$	empirical broadband spectrum
t	time
\vec{t}_1, \vec{t}_2	tangents to blade surface in spanwise and chordwise directions, respectively
T	period of signal or transfer function
$U(y)$	local Mach number in boundary layer
\vec{v}	velocity vector
$W(\zeta)$	complex velocity field around perfect circle
x	distance along chord or distance along airfoil surface measured from stagnation point
\vec{x}	observer position in media-fixed reference frame
\vec{y}	source position in media-fixed reference frame
z	complex plane of the airfoil section

Greek Symbols

α	blade section angle of attack
α'	angle-of-attack perturbation
$\beta_{.75}$	blade pitch at 3/4 span
δ_1	boundary layer displacement thickness
δ_2	boundary layer momentum thickness
δ_3	boundary layer energy thickness
ϵ	polar coordinate angle difference between near circle and perfect circle
η_1, η_2, η_3	pitch axis coordinates fixed to propeller. η_2 is the pitch axis and η_3 is the forward shaft axis
ζ'	complex plane of the airfoil section represented as a near circle
θ	angle between normal vector and radiation vector
Γ	circulation around airfoil section or curve of intersection of collapsing sphere and propeller blade surface
λ	advance ratio M_∞/M_t
ξ_1, ξ_2	blade surface coordinates. ξ_1 varies with span, ξ_2 varies with chord
ρ_∞	ambient density
σ	propeller solidity
τ	retarded time
ϕ	blade section inflow angle
ψ	elliptic blade thickness function
ω	angular frequency
Ω	propeller angular velocity

Subscripts

h	helical
i	induced
L	leading edge
r	refraction effect
s	scattering effect
S	stagnation point
tr	transition point
T	trailing edge

AERODYNAMIC PREDICTION

Geometry

While geometry is given rather than predicted, it is worthwhile to carefully consider the way geometric data are utilized. Two coordinates are required to specify a point on a surface. It is important to choose surface coordinates such that the functions of these coordinates will be single-valued and free of singularities at least up to their second derivatives, that is, functions of the surface coordinates will be of class C^2 . The selected surface coordinates should also provide a convenient computational grid.

Figure 2 shows the basic coordinate system $y_1y_2y_3$ used to describe the propeller. At time $t = 0$, a rotating coordinate system $\eta_1\eta_2\eta_3$ is congruent to the $y_1y_2y_3$ system. The shaft axis is η_3 , the blade pitch axis is η_2 , and the η_1 axis completes an orthogonal triad. Sections A-A through the blade at constant span positions give the first surface coordinate

$$\xi_1 = \eta_2 \quad (1)$$

At each section, a Joukowski transform (see reference 3, for example)

$$z = \zeta' + \frac{b^2}{\zeta'} \quad (2)$$

where

$$z = \eta_1 + i\eta_3, \quad (3)$$

and

$$\zeta' = b e^{\psi + i\xi_2} \quad (4)$$

is used to introduce the second surface coordinate ξ_2 . The blade surface elliptical coordinate $\psi(\xi_2)$ resulting from this transformation is shown in figure 3. The blade surface is described by the function $\psi(\xi_2)$. The blade surface is unwrapped by the Joukowski transform if the second surface coordinate ξ_2 is chosen to equal η_2 . The surface function $\psi(\xi_1, \xi_2)$ is single valued, continuous and slowly varying in the surface coordinates ξ_1, ξ_2 as shown in figure 3. The computation grid stretches the region near the

leading edge, $\xi_2 = \pi$, so that aerodynamic functions such as the coefficient of pressure C_p will be slowly varying in this region. In this computational space bicubic splines are suitable interpolating functions and will be used in all subsequent computations.

Potential Field

The potential flow field around each airfoil section $\xi_1 = \text{constant}$ is given by a conformal transformation of the flow around a perfect cylinder (reference 3). The blade geometry analysis has already produced part of the desired transformation by mapping the airfoil section in the z -plane as shown in figure 3. Recall that the airfoil thickness function $\psi(\xi_1, \xi_2)$ was generated by inverting the Joukowski transformation.

$$z = \zeta' + \frac{b^2}{\zeta'} \quad (5)$$

This transformation may now be used directly to map a given flow around the near-circle into a flow around the airfoil section.

Theodorsen's transformation (Ref. 4) maps the ζ -plane of the perfect circle into the ζ' -plane of the near circle

$$\zeta' = \zeta \exp \left\{ \sum_{n=1}^{\infty} \frac{C_n}{\zeta^n} \right\} \quad (6)$$

The constants C_n in Theodorsen's transformation are found from the shape of the airfoil in the ζ' -plane. After numerically solving for these constants, it is found that the trailing edge point of the airfoil is displaced by a small angle ϵ_T from the real axis of the ζ -plane. This point is required to be a stagnation point for the flow around the cylinder in order to satisfy the Kutta condition that trailing edge velocities are finite.

The complex flow function around the perfect circle is

$$W(\zeta) = M \left(e^{-i\alpha} - \frac{a^2}{\zeta^2} e^{i\alpha} \right) + \frac{i \Gamma}{2\pi\zeta} \quad (7)$$

where M is the local Mach number (for the section), α is the angle of attack, a is the radius of the circle, and Γ is the circulation. The trailing edge stagnation point is

$$\zeta_{ST} = a e^{i\epsilon_T}$$

which, with $W(\zeta_{ST}) = 0$, gives the circulation Γ as

$$\Gamma = 4\pi a M \sin(\alpha - \epsilon_T) \quad (8)$$

The leading edge stagnation point, a second solution to the equation $W(\zeta_S)$

is

$$\zeta_{SL} = a e^{i(2\alpha - \epsilon_T + \pi)} \quad (9)$$

The cross product of the velocity vector and the circulation vector gives the lift

$$C_L = 2\pi \left(\frac{4b}{c} \right) \sin(\alpha - \epsilon_T) \quad (10)$$

The coefficient of pressure is found from the velocity in the z -plane of the airfoil.

$$C_p = 1 - \left| \frac{W(z)}{M} \right|^2 \quad (11)$$

The complex velocity in the z -plane is found by using the derivatives of the transformations

$$W(z) = \left(\frac{d\zeta}{dz} \right) \frac{W(\zeta)}{\left(\frac{d\zeta}{dz} \right)}, \quad \zeta' \neq \zeta'_S \quad (12)$$

At the stagnation points in the ζ -plane, the limit of equation (12) is used.

$$W(z) = \left(\frac{dz}{d\zeta} \right) \lim_{\zeta' \rightarrow \zeta'_S} \frac{W(\zeta)}{\left(\frac{d\zeta'}{d\zeta} \right)} \quad (13)$$

Since the Joukowski transformation has a singularity at the trailing edge, $W(\zeta)$ will have a finite non-zero limit at this point. This causes the coefficient of pressure at the trailing edge to have magnitude less than one.

Figure 5 shows the blade section data computed by the blade section potential flow analysis. The coefficient of pressure C_p has a maximum of unity at the leading edge stagnation point ξ_{2S} . The lower surface C_p is generally positive, decreasing to a small value near the trailing edge $\xi_2 = 2\pi$ where the airfoil surface velocity is near the free-stream velocity. The upper surface C_p may become negative with high velocities around the highly curved leading edge. The upper surface C_p then approaches a small negative value at the trailing edge $\xi_2 = 0$. The lift coefficient C_L has a slope of approximately 2π when plotted as a function of α .

The function of the blade aerodynamics module is summarized as follows. Input is the blade shape function $\psi(\xi_1, \xi_2)$ and the parameters α and M . The module maps the flow around a perfect cylinder into the flow around the blade using the Theodorsen and Joukowski transforms. Outputs are the section lift coefficient C_L and leading edge stagnation point ξ_{2S} as a function of span position ξ_1 and the parameters α and M . The output coefficient of pressure depends on surface position (ξ_1, ξ_2) and the parameters α and M . The stagnation point location and the coefficient of pressure are used in the boundary layer analysis which follows.

Boundary Layer

The boundary layer module computes the two-dimensional boundary layer on each airfoil section as shown in figure 6. The blade arc length x is measured from the stagnation point on the leading edge. The initial portion of the boundary layer is laminar. Transition to turbulent flow occurs near the point where the external velocity $U(x)$ is a maximum. This turbulent layer continues to the trailing edge unless separation occurs.

The governing equations for the boundary layer thicknesses are the integral momentum equation for $\delta_2(x)$ and the integral energy equation for $\delta_3(x)$. The displacement thickness $\delta_1(x)$ is related to the momentum and energy thicknesses through the assumed profile $U(y)$ for the boundary layer.

The governing equations for $\delta_2(x)$ and $\delta_3(x)$ are

$$\frac{d\delta_2(x)}{dx} + \left(\frac{2+H_{12}}{U}\right) \frac{dU}{dx} \delta_2(x) = C_T \quad (14)$$

$$\frac{d\delta_3(x)}{dx} + \left(\frac{3}{U}\right) \delta_3(x) = C_D \quad (15)$$

The shape factor H_{12} is a given function of the thicknesses δ_2 and δ_3 and the external velocity gradient $\frac{dU}{dx}$. The coefficient C_T is the local wall shear stress coefficient and the coefficient C_D is the energy dissipation coefficient.

In the laminar layer, C_T is known from the assumed boundary layer velocity profile and equation (14) can be integrated to find $\delta_2(x)$ without solving for the energy thickness. Holstein and Bohlen's method (reference 5, Chapter X) is used to integrate this equation. Transition is assumed to occur when the external velocity is a maximum, that is, where

$$\frac{dU(x_{tr})}{dx} = 0 \quad (16)$$

Both equations must be integrated in the turbulent region. Truckenbrodt's method (reference 5, Chapter XXII) is used for this purpose. The coefficients C_T and C_D are given by empirical functions in the turbulent region.

The section profile drag coefficient is computed by Young and Squire's method (reference 5, Chapter XXV). In this method, the wake thickness at infinity is estimated by the empirical formula

$$\delta_{2\infty} = \delta_2(x_T) \left(\frac{U(x_T)}{U_\infty} \right)^{3.2} \quad (17)$$

and the section drag coefficient, referred to the chord, is

$$C_d = 2 \left(\frac{\delta_{2\infty}}{c} \right) \quad (18)$$

The boundary layer module computes the skin friction coefficient (see figure 7) C_f for use later in the blade loading module. It provides the drag coefficient C_d for propeller performance analysis and for the computation of lifting line (compact source) loads. The trailing edge thicknesses $\delta_1(x_T)$ and $\delta_2(x_T)$ are used in scaling laws for trailing edge broadband noise.

Propeller Performance

Computation of the propeller performance depends on a solution for the induced velocity field. This induced field at a blade section is shown in figure 8. Propeller performance is predicted by Lock's method (reference 6). The blade section aerodynamic module gives tables of section lift functions $C_l(\xi_1, \alpha, M)$. The boundary layer module gives tables of $C_d(\xi_1, \alpha, M)$.

These tables are used in the prediction of propeller performance coefficients C_p and C_T for given tip and forward Mach numbers M_t and M_∞ of the propeller.

The helical Mach number at a blade section (see figure 9) M_h is known from its components. These components are the axial Mach number of the propeller M_∞ and the rotational Mach number at the section $\xi_1 M_t$, where M_t is the tip rotational Mach number $R\Omega/c_\infty$. The local induced Mach vector M_i must be found to compute the total local Mach vector by

$$\vec{M} = \vec{M}_h + \vec{M}_i \quad (19)$$

This vector is represented by its magnitude M and the inflow direction angle ϕ as shown in figure 9. Differential components of lift dL and drag dD on the section are rotated through the inflow angle ϕ to give the differential thrust force dT and torque force dQ . These differentials are then integrated over the blade length and converted to performance coefficients: the torque or power coefficient C_p and the thrust coefficient C_T . The two components of the induced Mach vector are supplied by solving the two equations for the change of momentum in the far wake of the propeller. The increase in axial momentum, the value downstream minus the value upstream, is equal to the thrust force. The increase in angular momentum is equal to the propeller torque. These balance equations are

$$2M \sin \phi (M \sin \phi - M_\infty) F(\xi_1, \lambda) = \frac{1}{2} M^2 \sigma(\xi_1) [C_{\ell} \cos \phi - C_d \sin \phi] \quad (20)$$

$$2M \sin \phi (\xi_1 M_t - M \cos \phi) F(\xi_1, \lambda) = \frac{1}{2} M^2 \sigma(\xi_1) [C_{\ell} \sin \phi + C_d \cos \phi] \quad (21)$$

The factor of 2 on the left of these equations represents the fact that velocities in the far wake are twice those at propeller disk. The factor $M \sin\phi$ represents the mass flow through the disk. The factor $(M \sin\phi - M_\infty)$ in the thrust equation is the axial induced Mach number and the factor $(\xi_1 M_t - M \cos\phi)$ is the angular induced Mach number. The Prandtl circulation function (reference 7) $F(\xi_1, \lambda)$ is derived from vorticity theory. It is defined by

$$F = \frac{2}{\pi} \text{Arccos} \left\{ \exp \left[-\frac{N}{2} (1 - \xi_1) \frac{1 + \lambda^2}{\lambda} \right] \right\} \quad (22)$$

and is an approximate way of representing Goldstein's circulation function (reference 8). The above solution procedure was developed in 1930 by C. N. H. Lock (reference 6).

Loading

Blade loads are computed by combining results of the aerodynamics, boundary layer, and performance modules as shown in figure 10. The lift and drag coefficients are three-dimensional tables in terms of span position ξ_1 , angle of attack α , and Mach number M . The surface stress coefficients C_p and C_f are four dimensional tables in terms of surface position ξ_1 and ξ_2 , angle of attack α , and section Mach number M . The performance analysis produces actual values $\alpha(\xi_1)$ and $M(\xi_1)$ for the propeller operating conditions M_∞, M_t . There may be an additional angle-of-attack perturbation $\alpha'(\xi_1, t)$ due to small nonuniformities in the propeller inflow.

When the stress and loading coefficient tables are interpolated with these functions, the coefficients became actual time-dependent values

$$C_l(\xi_1, t) = C_l[\xi_1, \tilde{\alpha}(\xi_1, t), M(\xi_1)] \quad (23)$$

$$C_d(\xi_1, t) = C_d[\xi_1, \tilde{\alpha}(\xi_1, t), M(\xi_1)] \quad (24)$$

$$C_p(\xi_1, \xi_2, t) = C_p[\xi_1, \xi_2, \tilde{\alpha}(\xi_1, t), M(\xi_1)] \quad (25)$$

$$C_f(\xi_1, \xi_2, t) = C_f[\xi_1, \xi_2, \tilde{\alpha}(\xi_1, t), M(\xi_1)] \quad (26)$$

where

$$\tilde{\alpha}(\xi_1, t) = \alpha(\xi_1, t) + \alpha'(\xi_1, t) \quad (27)$$

Replacing the parametric arguments α and M by actual arguments reduces the lift and drag tables to two dimensions and the stress coefficient tables to three dimensions. If steady loadings are assumed, the loading tables are reduced by a further dimension. These loading tables are passed to the discrete noise prediction module for noise prediction. The line loads $C_l(\xi_1, t)$ and $C_d(\xi_1, t)$ are used in compact source theories and the distributed loads $C_p(\xi_1, \xi_2, t)$ and $C_f(\xi_1, \xi_2, t)$ are used in the general non-compact source theories. A similar transformation of the boundary layer thicknesses is used to supply data to the broadband noise prediction module.

ACOUSTIC PREDICTION

Discrete Tone Noise

Subsonic Noise.- Discrete tone noise is predicted by Farassat's method (reference 9). Farassat's equation for the noise of a subsonic propeller is

$$4\pi p(x,t) = \frac{\partial}{\partial t} \int_{\text{blade}} \left[\frac{M_n + \ell_r}{r|1-M_r|} \right]_{\tau} dS + \int_{\text{blade}} \left[\frac{\ell_r}{r^2|1-M_r|} \right] dS \quad (28)$$

The terms in equation (28) are illustrated in figure 11. Pressure is computed at a particular observer position \vec{x} and time t . Two integrals are evaluated to give the total pressure. The integrals are over the surface area of the propeller blade and the integrands are evaluated at the time τ when the sound is emitted at the surface position $\vec{y}(\tau)$. The radiation vector \vec{r} is the difference between the observer and source positions

$$\vec{r} = \vec{x}(t) - \vec{y}(\tau) \quad (29)$$

The normal vector \vec{n} and surface area dS are given by

$$\vec{n}dS = \frac{\partial \vec{n}}{\partial \xi_1} \times \frac{\partial \vec{n}}{\partial \xi_2} \quad (30)$$

and the velocity vector is

$$\vec{v} = \vec{M}_{\infty} + \vec{\Omega} \times \vec{n} \quad (31)$$

The loading vector is

$$\vec{\ell} = \frac{M^2}{2} (\pm C_f \vec{t}_2 + C_p \vec{n}) \quad (32)$$

where the positive sign is used on the lower surface between the stagnation point on the lower surface and the trailing edge. The base vector \vec{t}_2 is tangent to the surface and in the chordwise direction. A unit vector in the radiation direction \vec{r} is used to define

$$M_r = \vec{r} \cdot \vec{v} \quad (33)$$

and

$$l = \vec{r} \cdot \vec{l} \quad (34)$$

Integration of equation (28) is straightforward except for the solution for retarded time. The basic retarded time equation requires the distance from the source to the observer to be compatible with the propagation time

$$\vec{r} \cdot \vec{r} = |\vec{x}(t) - \vec{y}(\tau)|^2 = (t - \tau)^2 \quad (35)$$

In the case of a propeller moving along its own axis, the retarded time equation can be reduced to

$$A_0(t-\tau)^2 + 2B_0(t-\tau) + C_0 + C_1 \cos\tau = 0 \quad (36)$$

Equation (36) has the appearance of a quadratic equation in $(t-\tau)$ except for the coefficient $C = C_0 + C_1 \cos\tau$. It can be shown, however, that there is a single real solution $\tau < t$ to this equation as long as the motion of the propeller is subsonic.

Transonic noise.- Supersonic noise is computed by Farassat's collapsing sphere method. The subsonic equation cannot be used on any portion of the blade when M_r may exceed unity because of the $|1-M_r|$ singularity. In addition, the retarded time equation has multiple roots. The collapsing sphere method is illustrated in figure 12. The collapsing sphere intersects the blade surface in a curve called the Γ -curve. Farassat has shown that

$$\frac{dS}{|1-M_r|} = \frac{d\Gamma d\tau}{\sin\theta} \quad (37)$$

The integrals for noise are thus evaluated by choosing a set of times τ and integrating first along the Γ curves with fixed source time and then over source time. This method was developed by Nystrom and Farassat in reference 10.

Recent advances.—The time derivative $\frac{\partial}{\partial t}$ in Farassat's acoustic equation increases the computation time because at least two integrals must be evaluated to numerically compute the derivative. Numerical differentiation also introduces some spurious wiggles in the pressure signature which appear as increases in the higher harmonics of the transformed signal. Recently, Farassat (reference 11) has taken the derivatives inside the integral for both the subsonic and supersonic cases. The differentiation under the integral has shown that the noise depends on blade surface curvatures. The full implications of this exciting new result are not completely known at this time and are a subject of continuing research.

Broadband Noise

Broadband noise is generated by turbulence convected past the trailing edge of the airfoil as shown in figure 13. The mean-square pressure spectrum is given by Schlinker and Amiet as

$$\langle p^2(\vec{x}, \omega) \rangle = \int_{\text{trailing edge}} \frac{1}{4} \left[\left(\frac{k_x M z C}{2\pi \sigma^2} \right) |L|^2 \ell_y(\omega) S(\omega) \right] ds \quad (38)$$

where

$$k_x = \frac{\omega}{U} \quad (39)$$

and

$$\sigma = [x^2 + \beta^2(y^2 + z^2)]^{1/2} \quad (40)$$

The function L is the "effective lift" function derived by Amiet (reference 12) for an observer at retarded position (x, y, z) . The function $\ell_y(\omega)$ is an empirical correlation length

$$\ell_y(\omega) = \frac{2.1 U_c}{\omega} \quad (41)$$

where U_c is the turbulence convection velocity which is about $0.8 U$.

The spectrum function $S(\omega)$ is an empirical function for the blade surface pressure spectrum at the trailing edge.

$$S(\omega) = 2 \times 10^{-5} \left(\frac{1}{2} \rho_\infty U^2 \right)^2 \frac{\delta_1}{U} F(\omega) \quad (42)$$

where

$$\tilde{\omega} = \frac{\omega \delta_1}{U}$$

and

$$F(\tilde{\omega}) = 33.28 \tilde{\omega} (1 - 5.49 \tilde{\omega} + 36.7 \tilde{\omega}^2 + 0.151 \tilde{\omega}^4)^{-1} \quad (43)$$

Nearfield Effects

Two effects are present in the nearfield of the propeller which may significantly alter the received noise. These effects are the scattering by the aircraft's wings and fuselage and the refraction by the boundary layer on the surface of the aircraft.

Scattering. The scattering effect is illustrated in figure 14 for a cylindrical fuselage. The free field levels on the surface of a cylindrical fuselage are calculated by one of the previously described methods for discrete noise. This incident field $p_i(\omega, \theta, x)$ is transformed by

$$p_i(\omega, m, k_x) = \frac{1}{2\pi} \int_0^{2\pi} \int_{-\infty}^{\infty} e^{-i(k_x x + m\theta)} p_i(\omega, \theta, x) dx d\theta \quad (44)$$

to give the incident field in a wavenumber space. The solution for the total pressure on the fuselage surface can then be found by superimposing the general solutions for incident and scattered cylindrical waves such that the boundary condition

$$\left. \frac{\partial p(\omega, m, k_x)}{\partial r} \right|_{r=a} = 0 \quad (45)$$

is satisfied. The result for the total surface pressure can be given by a transfer function.

$$p_t(\omega, m, k_x) = 2T_s(\omega, m, k_x) p_i(\omega, m, k_x)$$

where

$$T_s(\omega, m, k_x) = \left\{ -\frac{i\pi k_r a}{2} \frac{(1)'}{H_m(k_r a)} \frac{(2)}{H_m(k_r a)} \right\}^{-1} \quad (47)$$

and

$$k_r = (\omega^2 - k_x^2)^{1/2} \quad (48)$$

The factor of 2 in equation (46) is shown explicitly to represent the effect of pressure doubling. With this form, the transfer function for scattering approaches unity for high frequencies as may be seen from the asymptotic forms for the Hankel functions. Following the computation of total pressure p_t in wavenumber space, an inverse transform is used to find the surface pressure as a function of position (θ, x) .

Refraction.- The boundary layer velocity profile alters the sound pressure level on the surface of the fuselage by turning the waves propagated upstream away from the surface and turning waves propagated downstream into the surface. This effect is depicted in figure 15. This refraction effect is small for aircraft in low speed flight but becomes significant at the higher subsonic Mach numbers.

A simple model of the refraction effect neglects scattering and uses the two-dimensional wave equation in a sheared flow as the basis for finding a transfer function. The sheared-flow wave equation is

$$(\omega - Uk_x) \frac{d^2 p}{dy^2} + 2 \left(\frac{dU}{dy} \right) k_x \frac{dp}{dy} + (\omega - Uk_x) [(\omega - Uk_y)^2 - k_x^2] p = 0 \quad (49)$$

This equation can be integrated, given the boundary layer velocity profile $U(y)$, from the surface where $y = 0$ to the edge of the boundary layer where $y = \delta$. Initial conditions at the surface are an assumed unit pressure

$$p(0) = 1 \quad (50a)$$

and

$$\frac{dp(0)}{dy} = 0 \quad (50b)$$

Integrating equation (49) with initial conditions (50) gives the pressure p_δ and velocity v_δ at the edge of the boundary layer. These results must be scaled to match the pressure in the known incident wave field. The process of matching the incident field produces a transfer function for refraction

$$T_r(\omega, k, k_x) = \frac{k_y}{k_y p_\delta(\omega, k_x) - (\omega - Uk_x) v_\delta(\omega, k_x)} \quad (51)$$

Numerical integration of the sheared flow equation breaks down at the regular singular point $(\omega - Uk_x) = 0$ which corresponds to the coincidence of wave speed with flow speed in the boundary layer. Special techniques beyond the scope of this paper have been used to integrate the sheared-flow wave equation (49) in these cases.

Combined effects.- The combined effects of scattering and refraction may be found by integrating the sheared-flow equation in cylindrical coordinates to find the cylindrical wave pressure p_δ and velocity v_δ at the edge of the boundary layer. Matching the external field then gives a combined transfer function

$$T_{sr}(\omega, m, k_x) = \frac{k_r}{\left\{ \left[-i \left(\frac{\pi z}{2} \right) H_m^{(1)}(z) H_m^{(2)}(z) \right] k_r p_\delta - \left[\left(\frac{\pi z}{2} \right) H_m^{(1)}(z) H_m^{(2)}(z) \right] (\omega - Mk_x) v_\delta \right\}} \quad (52)$$

where

$$z = k_r(a + \delta) \quad (53)$$

Farfield Effects

Noise propagated to the farfield is modified by the effects of atmospheric attenuation and ground reflections and attenuation. Since phase information tends to be lost after propagation over long distances, farfield noise effects are applied to the mean-squared pressure spectrum of the noise rather than to the pressure itself (reference 2).

Atmospheric attenuation.- The effect of atmospheric attenuation is computed by the ANSI method described in reference 2. The mean-squared pressure on a source sphere of fixed radius r_s is reduced by the spherical spreading effect and atmospheric attenuation. The transfer function for attenuation T_a is a decaying exponential function $\exp(-2\alpha r)$. The attenuation rate α is a function of frequency. The lower frequencies are dominated by the effect of nitrogen relaxation. Mid-frequencies are usually dominated by oxygen relaxation effects and the higher frequencies are dominated by the classical absorption effects of conductivity, viscosity, and rotational modes of molecular vibration. The ANSI-proposed standard method is used for the calculation of attenuation effects for both standard and non-standard conditions.

Ground effects.- The farfield noise is reflected and attenuated by the ground. This effect may be represented in the transfer function T_g developed by Pao, Wenzel, and Oncley in reference 13. This transfer function is based on the complex reflection coefficient $Re^{i\phi}$ for a spherical wave over an impedance plane. The factor R is the magnitude of the reflection which is equal to or less than unity. The factor ϕ is the phase shift between the reflected and incident waves. The magnitude of the noise at the observer depends on the difference in the lengths of the direct ray path and the,

reflected or image ray path. The magnitude of the received noise is diminished slightly by the loss of coherence of the direct and reflected signals. This coherence loss also depends on the path length difference.

COMPARISONS TO EXPERIMENTS

Subsonic Propeller

Noise predicted by this system has been compared to noise measured during the flight of the twin-engined aircraft shown in figure 16. The aircraft was fitted with a wing-mounted microphone boom which could be moved to measure the noise in front of and behind the propeller plane. Noise was also measured on the ground with level flights over the measurement point.

Propeller performance.- An intermediate check of the prediction system was made by Block and Martin (reference 14) using a 1/4-scale model of the twin aircraft's propeller on the propeller test stand (figure 17) at Langley Research Center.

Computed and measured power coefficients are shown in figure 18 as a function of advance ratio $J = V_\infty/nD$ and 3/4 span pitch setting $\beta_{.75}$. The predicted power coefficient is near the measured values at the lower pitch settings but rises above the measured power at the higher settings where it is believed that the propeller is in a condition of partial stall. Similarly, the predicted thrust coefficient C_T (figure 19) is above the measured value with fair agreement at the low pitch settings and poor agreement at the high pitch and thrust values.

Effective pitch.- Pitch was not measured during the flight of the aircraft when the noise was measured. In order to find an effective value for the pitch setting $\beta_{.75}$ to use in noise predictions, the measured power in flight was used to compute the power coefficient C_p . An effective pitch setting $(\beta_{.75})_{eff}$ was then found such that the predicted power coefficient matched the measured value. This effective pitch will be less than the pitch setting on the 1/4-scale model for the same C_p .

Propeller noise. Nearfield noise measured in flight is shown in figure 20. The measured noise data were sampled using data blocks of 96 time points per shaft revolution which gave 32 points per blade for the three-bladed prop. Fifty blocks of data were ensemble averaged to find the mean signal $p(t)$ shown in figure 20. Signal number 1 is for one-third of a propeller revolution. Signals 2 and 3 which complete the revolution are similar. The standard deviation $\sigma(t)$ was nearly constant, indicating that the measured noise could be decomposed into discrete and random parts

$$p(t) = \bar{p}(t) + p'(t) \quad (54)$$

where $p'(t)$ is a stationary random signal. Sound pressure spectra were generated for each data block and for the ensemble-averaged data. The discrete spectrum $|\bar{p}(\omega)|^2$ and the random spectrum $|p'(\omega)|^2$ are added to give the total spectrum $|p(\omega)|^2$.

$$|p(\omega)|^2 = |\bar{p}(\omega)|^2 + |p'(\omega)|^2 \quad (55)$$

The spectral data shown in figure 21 are relative to the overall mean-squared pressure

$$\langle \bar{p}^2 \rangle = \lim_{T \rightarrow \infty} \frac{1}{2T} \int_{-T}^T \bar{p}^2(t) dt \quad (56)$$

The overall mean-squared pressure in figure 21 is within 1.8 dB of the measured value. This agreement may be due in part to the matching of power through the effective pitch setting procedure.

The predicted spectrum agrees well with the data for the first few harmonics. Starting at about the 5th harmonic, the measured discrete spectrum shows a cyclic pattern suggestive of cancellation and reinforcement which is

not predicted. This pattern gives levels from the 10th and 15th harmonics which are as much as 20 dB above the predicted values. A significant part of this underprediction is probably due to the omission of unsteady loads in the analysis. Despite these high-frequency errors, the predicted A-weighted sound pressure level will be in good agreement with the measured values because of the rapid decay of the levels with frequency.

The error in the discrete spectrum may be due to any of several effects, including the obvious possibility of an error in the prediction method. Scattering from the wing and fuselage was not included in these computations. Computations are made for one propeller and there may be a small contribution from the second propeller which contributes to the error.

In making the predictions, it was assumed that all blades are identical, whereas, in practice, there are slight blade-to-blade differences which may result in the reinforcement patterns seen here. There is regrettably no way to examine these possible sources of error without further detailed experimentation.

Farfield noise from the flyover of the twin prop aircraft is shown in figures 22 and 23. The limited amount of data shown in figure 22 are for flyovers with the reception angle $\theta = 90^\circ$ being the directivity angle when the sound is received. The prediction is 5 to 6 dBA above the average of the measured levels. The reason for the overprediction is shown in figure 23. The level for the first harmonic, which dominates the predicted source spectrum, is indicated by the data to be less than the second harmonic. The reason for this effect is unknown and a much larger data set should be examined before any conclusions are drawn. Flyover noise data for propellers typically scatter over a range of about 10 dB (see reference 15) so that statistical methods must be used to assess the accuracy of predictions.

Advanced Turboprop

Predictions have been made for the eight-bladed advanced turboprop propeller designated as SR-3. Since this propeller was operating at transonic conditions, the elementary aerodynamics and loading methods described earlier could not be used. A loading distribution was estimated by the propeller manufacturer and this distribution was adjusted such that the computed power matched the power measured during the flight test of the propeller.

The propeller was tested in flight atop the Jetstar aircraft shown in figure 24. Performance data were also obtained in the wind tunnel as shown in figure 25. Microphones were mounted in the surface of the fuselage along a line under the axis of the propeller. Measured noise data were reduced using ensemble-averaging techniques as described earlier. Only the results of the discrete noise data and predictions will be shown here.

Figure 26 shows a comparison of the measured and predicted noise at the cruise Mach number of 0.80. The helical Mach number of the blade tip is 1.13 for this example. Levels shown are for the blade passing harmonic which, remembering the subsonic results, is expected to give the best agreement with the measured data. Nystrom and Farassat's PROPFAN (reference 10) program was used to predict the freefield noise at the top of the boundary layer. The boundary layer profile was measured with rakes mounted on the fuselage of the Jetstar. The two-dimensional transfer function for the boundary layer was then used to predict the noise on the surface beneath the boundary layer. It is apparent that the boundary layer has a significant effect on the surface noise at this flight speed. The predictions agree better with the data both in front of and behind the plane of the propeller.

The causes of the discrepancy between predicted and measured levels on the Jetstar just behind the prop plane are being investigated at this time.

The scattering effect given by equation (47) will be evaluated first to see how scattering modifies the predicted surface pressures in the absence of a boundary layer. Following this the combined effects of scattering and refraction will be computed using the transfer function (52).

CONCLUDING REMARKS

NASA's ANOPP system for predicting propeller noise has been described here. The objective of this system is to predict noise directly from the shape and motion of the propeller blades. This objective requires aerodynamic computations to be made as a basis for the acoustic computations. The aerodynamic theories used here are simple classical methods.

These methods overpredict the performance of the propellers which results in an error in the acoustic predictions. An empirical correction procedure of matching predicted and measured power was used here to compensate for the known error in aerodynamic performance. The acoustic predictions give good agreement with the low-frequency discrete noise when they are adjusted by the power matching procedure. It is believed that improved aerodynamic theories will give good low-frequency predictions for subsonic propellers without an empirical correction for power.

The accuracy of the acoustic predictions decreases with increasing frequency. Errors of 10 dB or more may occur at or above the 10th harmonic of the blade passing frequency in the case of subsonic propellers. When the propeller has nearly steady loading, these errors do not seriously affect integrated measures of noise such as the A-weighted sound pressure level because the A-level is dominated by lower harmonics. The prediction methods used here are believed to be adequate for subsonic propellers operating in a tractor configuration where the loads are nearly steady. There is a need for

further investigation of noise from subsonic propellers operating as pushers where the unsteady loads will increase the levels of the higher harmonics relative to the fundamental.

Nearfield effects of scattering and boundary layer refraction significantly alter the noise levels of the fuselage of the aircraft. The boundary layer refraction effect reduces the surface noise in front of the propeller and increases the noise behind the propeller. This effect is significant for an aircraft with high subsonic Mach number such as the 0.80 Mach number envisioned for advanced turboprop-powered aircraft. The two-dimensional model of the boundary layer fails to explain a significant discrepancy between predicted and measured data just behind the plane of the SR-3 turboprop on the Jetstar aircraft. Three-dimensional refraction and scattering effects are being studied in an attempt to resolve this discrepancy.

Farfield effects of atmospheric attenuation and ground reflections modify the noise measured during the flyover of a propeller aircraft. The largest effect is that of ground reflection which introduces the "ground-dip" in the measured flyover noise. Available theories and methods are adequate for predicting these effects when the ground reflection angle is large. Although measurements from outdoor flyover tests have a typically large scatter of data, the flyover noise from propellers can usually be predicted within a standard deviation of about 4 dB.

1. Gillian, Ronnie E., Brown, Christine G., Bartlett, Robert W., and Baucom, Patricia H.: ANOPP Programmer's Reference Manual for the Executive System. NASA TM X-74029, 1977.
2. Zorumski, William E.: Aircraft Noise Prediction Program Theoretical Manual. NASA TM 83199, 1981.
3. Karamcheti, Krishnamurty: Principles of Ideal-Fluid Aerodynamics. John Wiley and Sons, Inc. New York/London/Sydney, 1966.
4. Theodorsen, T., and Garrick, I. E.: General Potential Theory of Arbitrary Wing Sections, NASA TR 452, 1933.
5. Schlichting, Hermann: Boundary-Layer Theory. 7th Ed., McGraw-Hill, 1968.
6. Lock, C. H. N.: Application of Goldstein's Theory to Airscrew Theory and Design. A. R. C. R&M No. 1377, 1930.
7. Glouert, H.: Airplane Propellers. Aerodynamic Theory, vol. IV, Division T., W. F. Durand, Editor-in-Chief.
8. Goldstein, S.: On the Vortex Theory of Screw Propellers. Proc. Royal Soc. A, vol. 123, 1929.
9. Farassat, F.: Theory of Noise Generation from Moving Bodies with an Application to Helicopter Rotors. NASA TR R-451, 1975.
10. Nystrom, Paul A., and Farassat, F.: A Numerical Technique for Calculation of the Noise of High-Speed Propellers with Advanced Blade Geometry. NASA TP 1662, July 1980.
11. Farassat, F.: The Prediction of the Noise in Supersonic Propellers in Time Domain - New Theoretical Results. AIAA Paper 83-0743, April 1983.
12. Schlinker, Robert H., and Amiet, Roy K.: Helicopter Rotor Trailing Edge Noise. NASA CR 3470, November 1981.
13. Pao, S. Paul, Wenzel, Alan R., and Oncley, Paul B.: Prediction of Ground Effects on Aircraft Noise. NASA TP 1104, 1978.
14. Block, P. J. W., and Martin, R. M.: Results from Performance and Noise Tests of Model Scale Propellers. SAE No. 83-0730. Presented at the 1983 SAE Business Aircraft Meeting and Exposition, Wichita, KS, April 12-15, 1983.
15. Heller, Hanno: Propeller Aircraft Noise-Certification and Flight-Testing. DFVLR-Mitt. 82-16, November 1982.

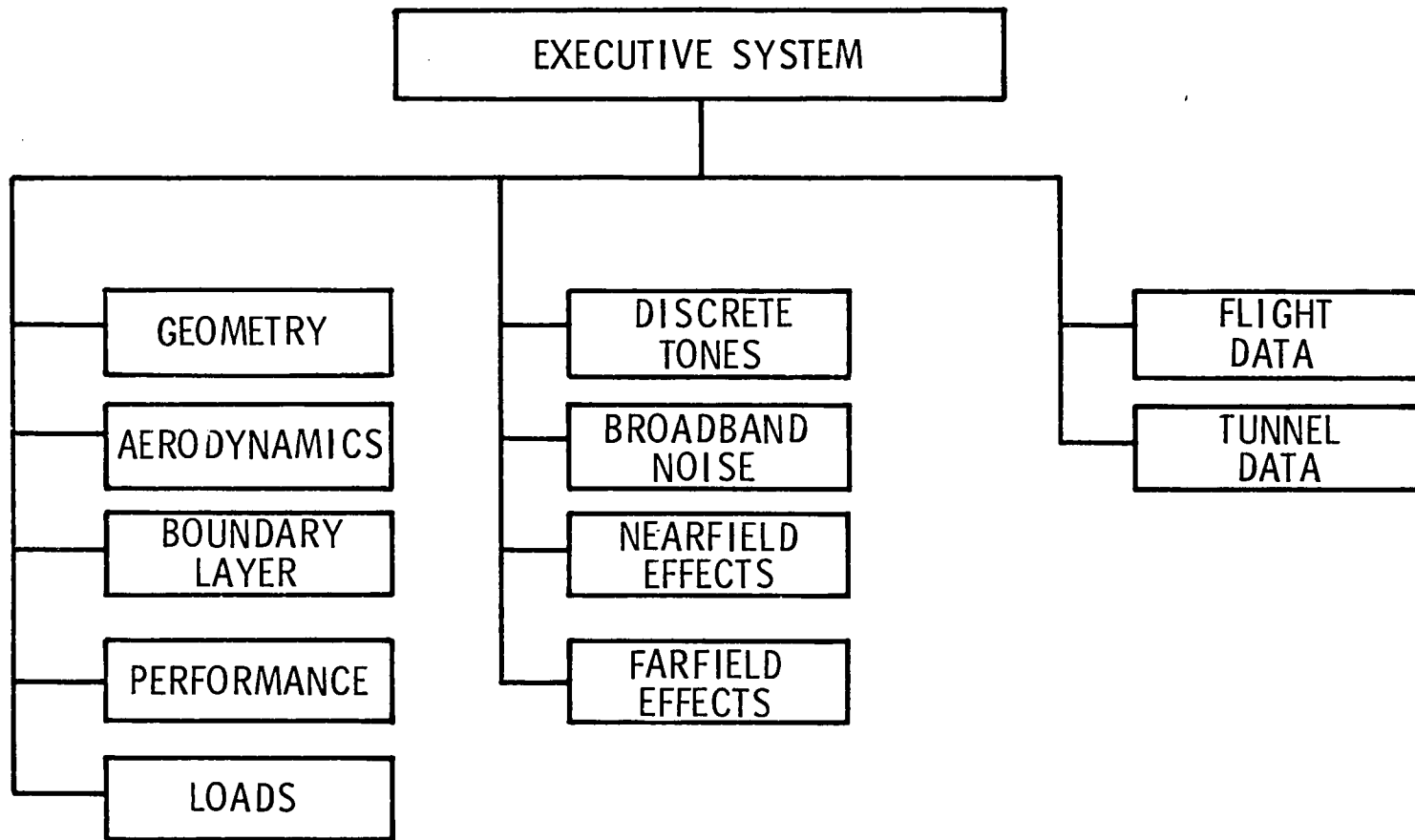


Figure 1.- ANOPP propeller noise prediction system.

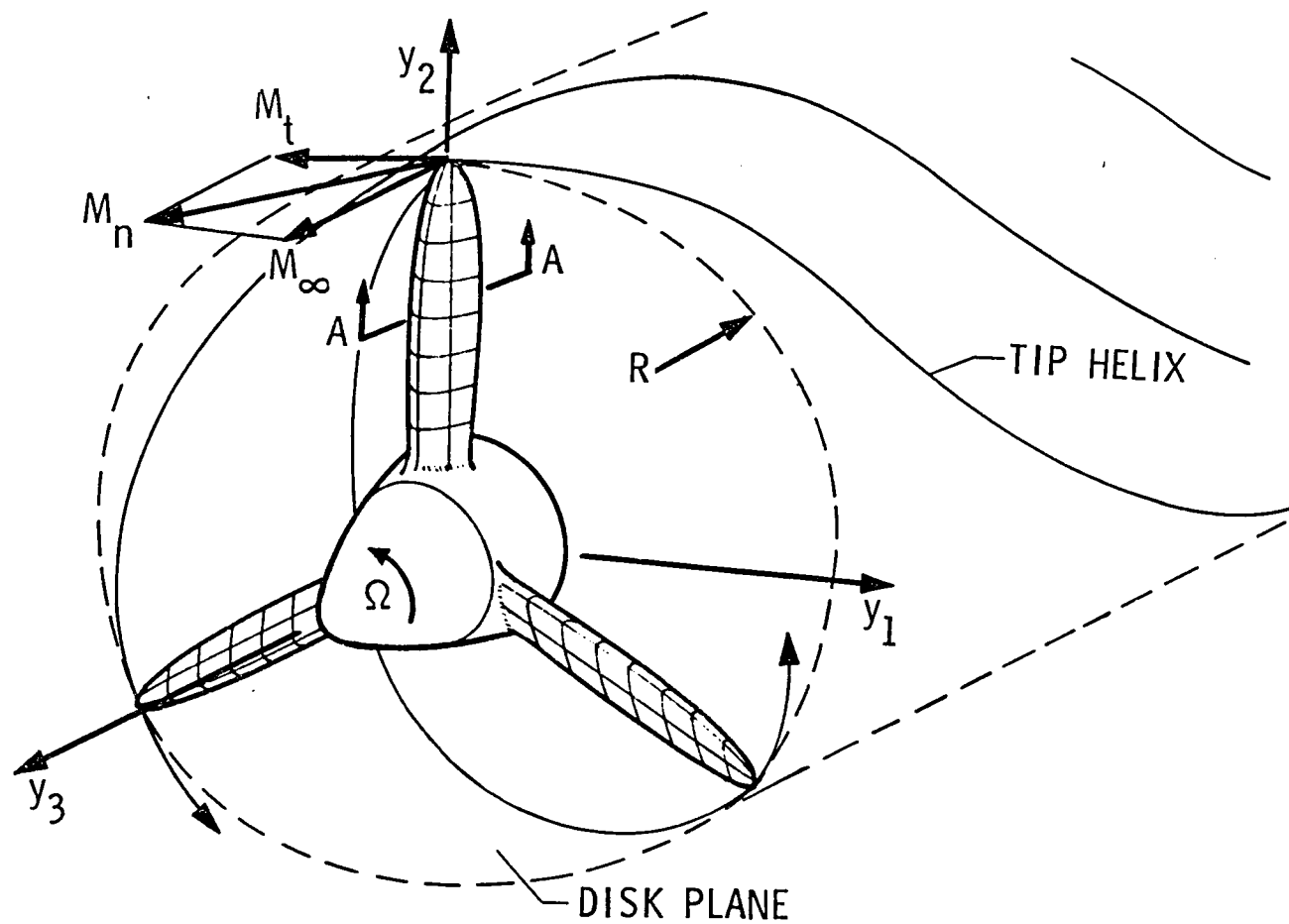
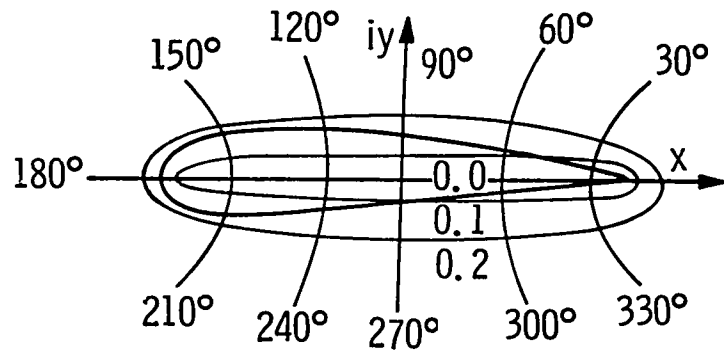
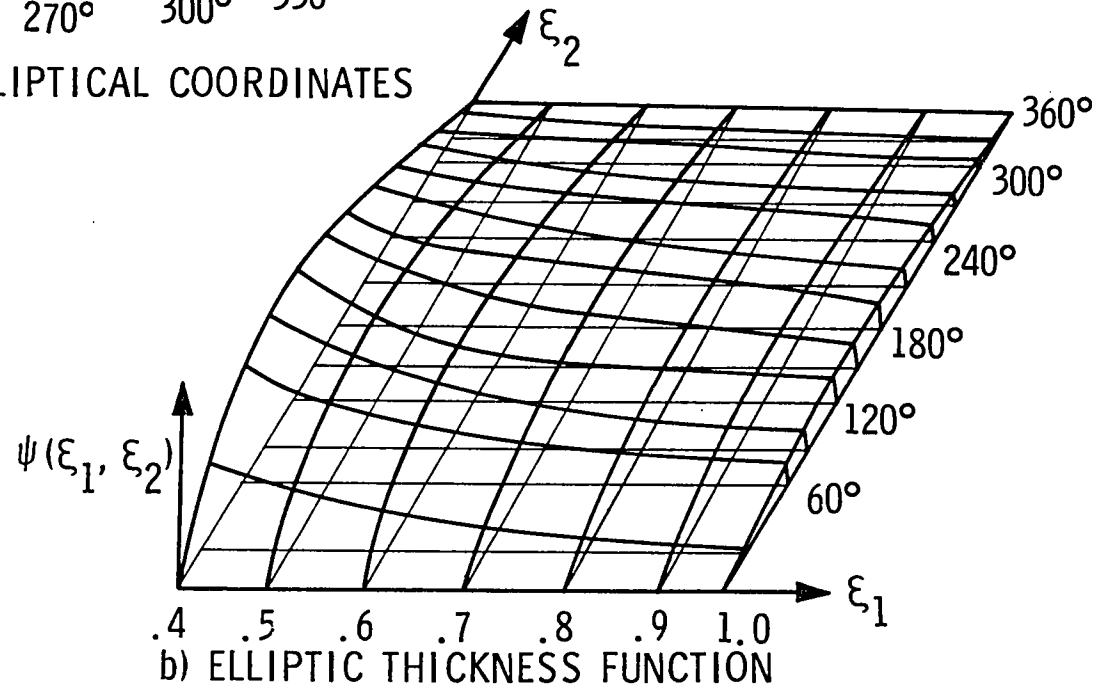


Figure 2.- Aircraft propeller geometry and motion.



a) SECTION A-A ELLIPTICAL COORDINATES



b) ELLIPTIC THICKNESS FUNCTION

Figure 3.- Propeller blade shape in surface coordinate system.

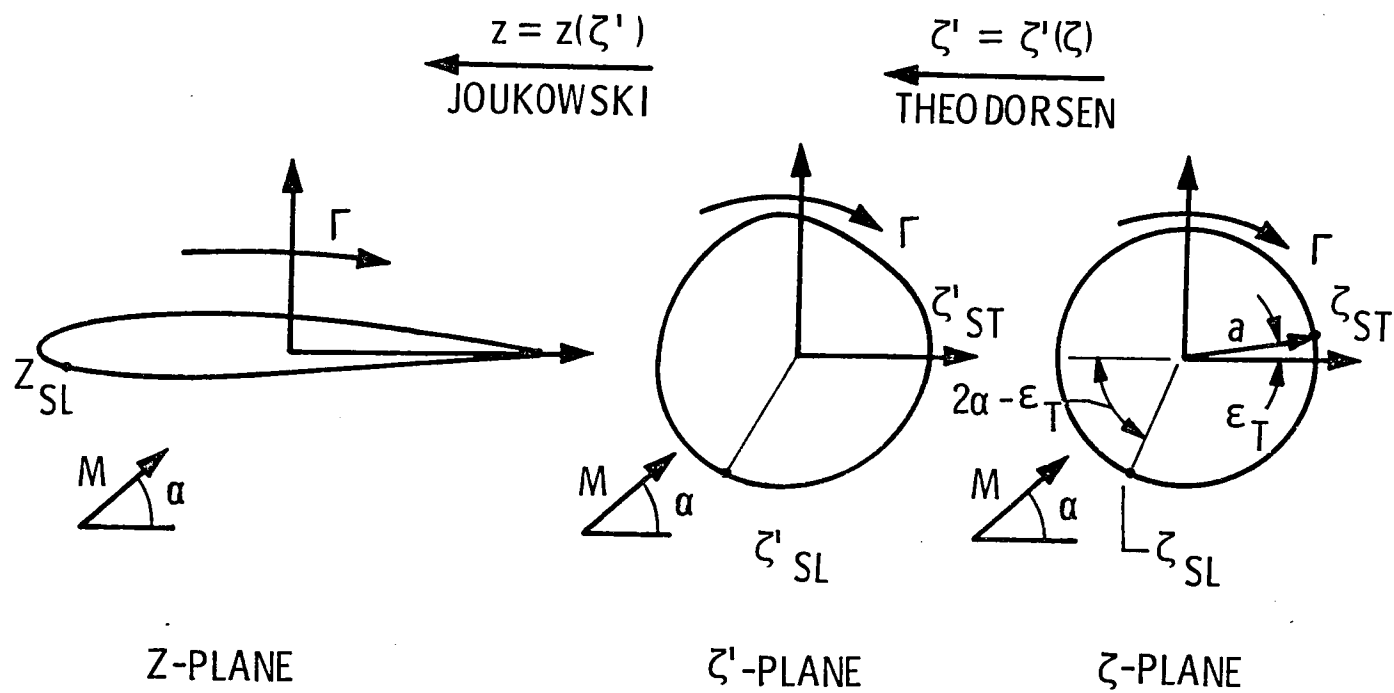


Figure 4.- Potential flow mapping for blade section.

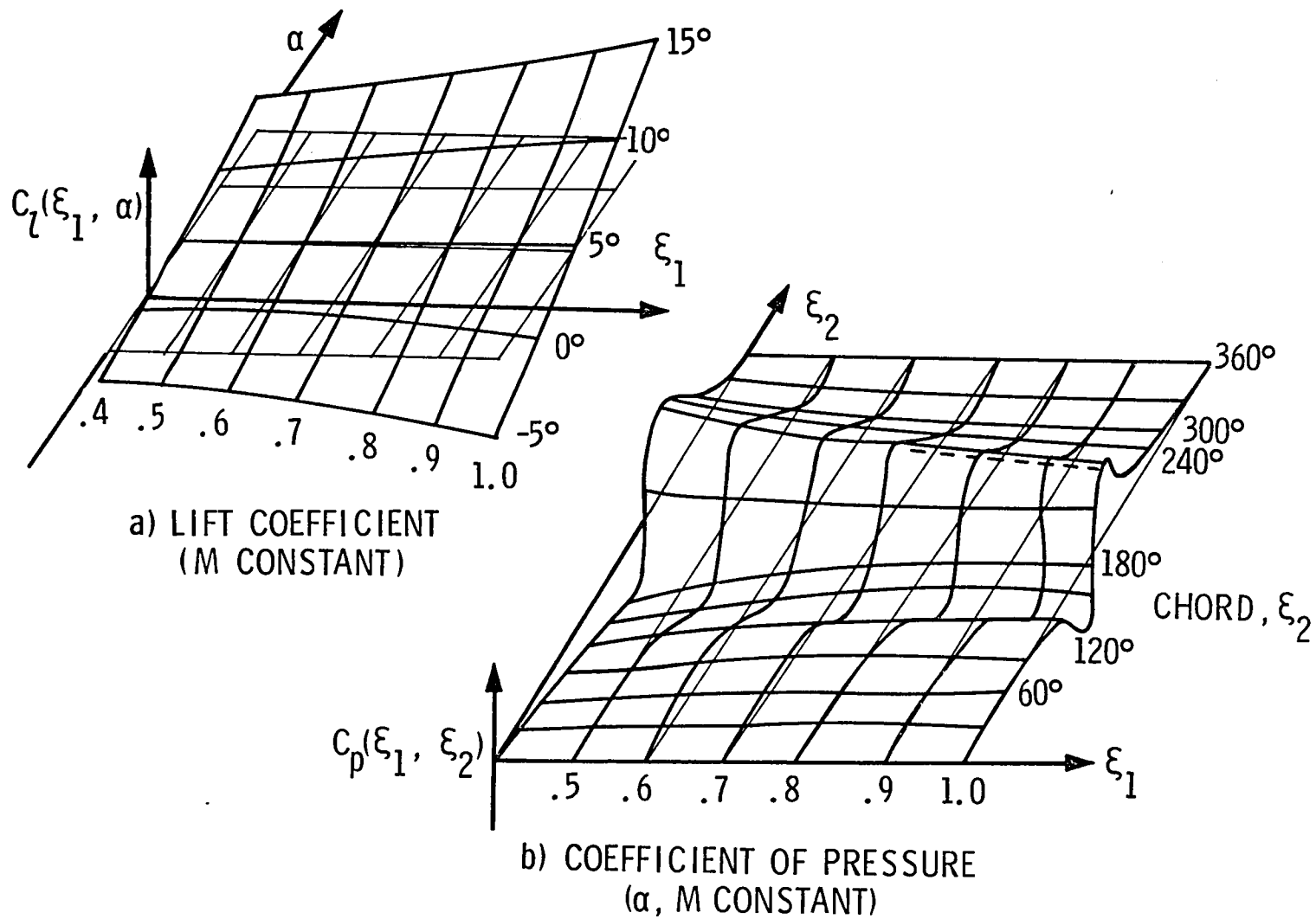


Figure 5.- Propeller blade lift and pressure coefficient functions.

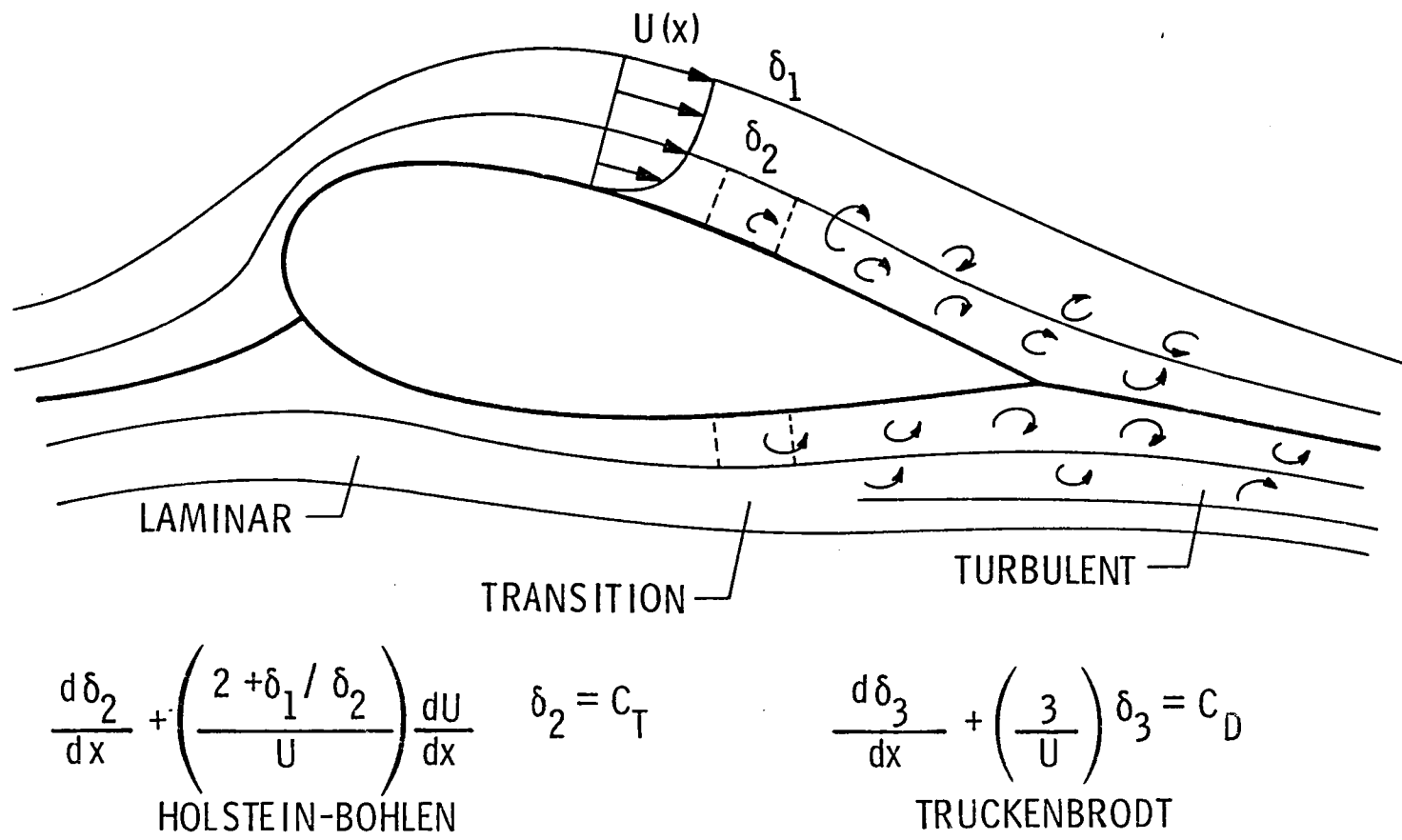


Figure 6.- Airfoil boundary layer analysis.

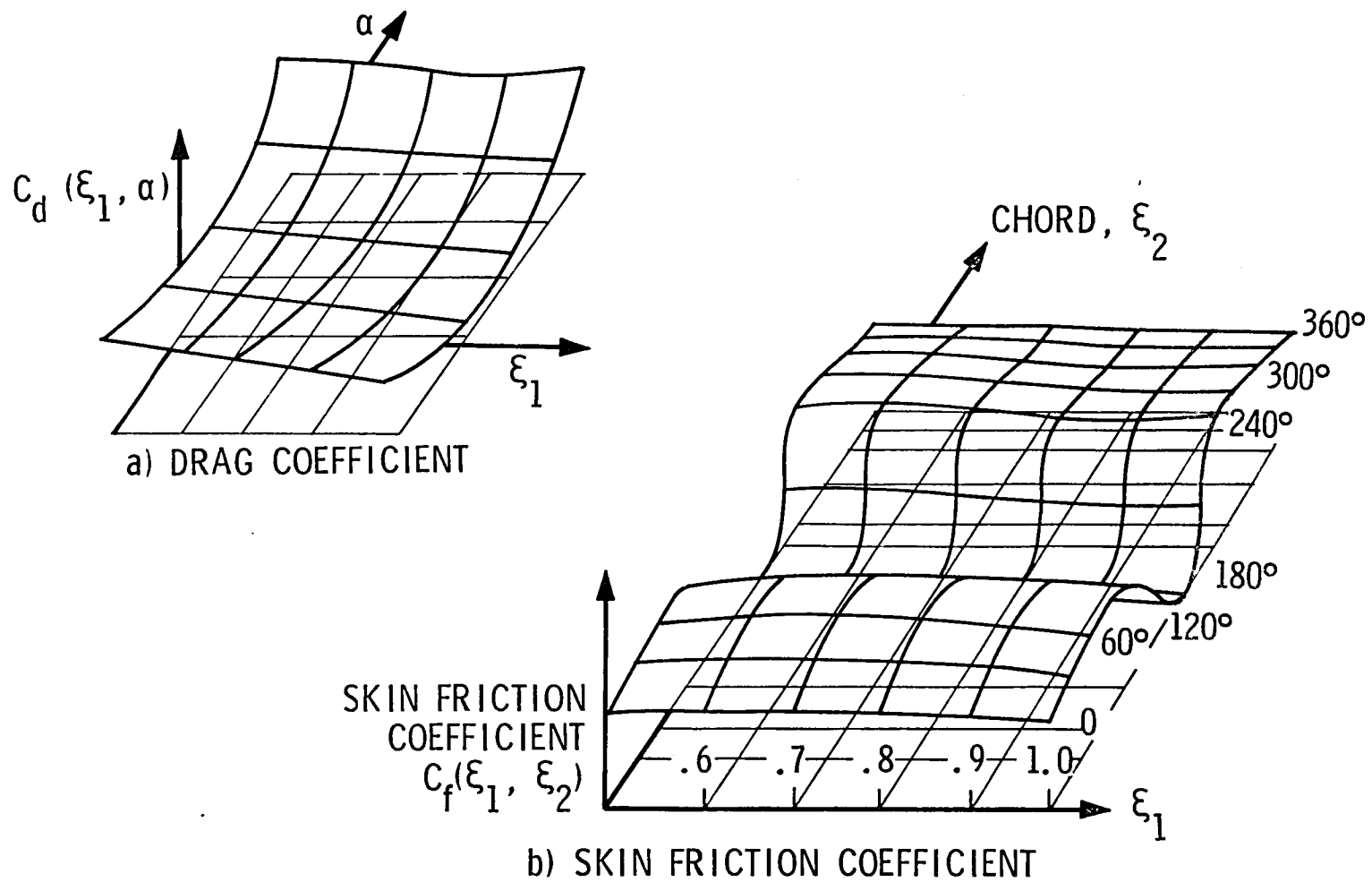


Figure 7.- Propeller blade drag and skin friction coefficient functions.

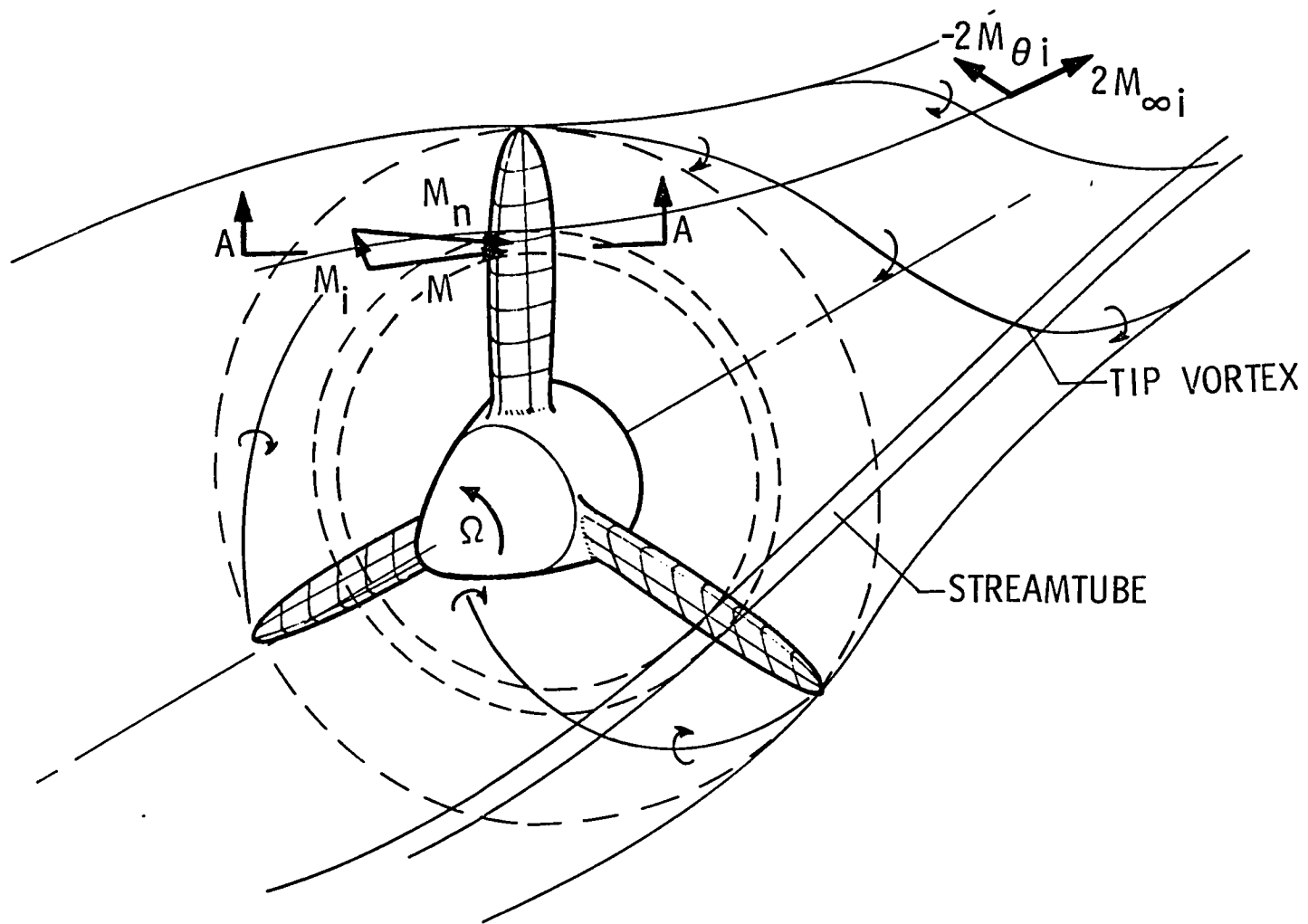


Figure 8.- Propeller induced flow.

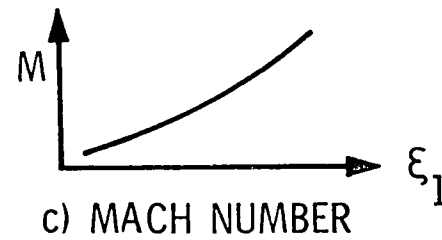
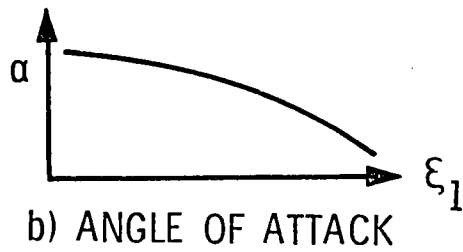
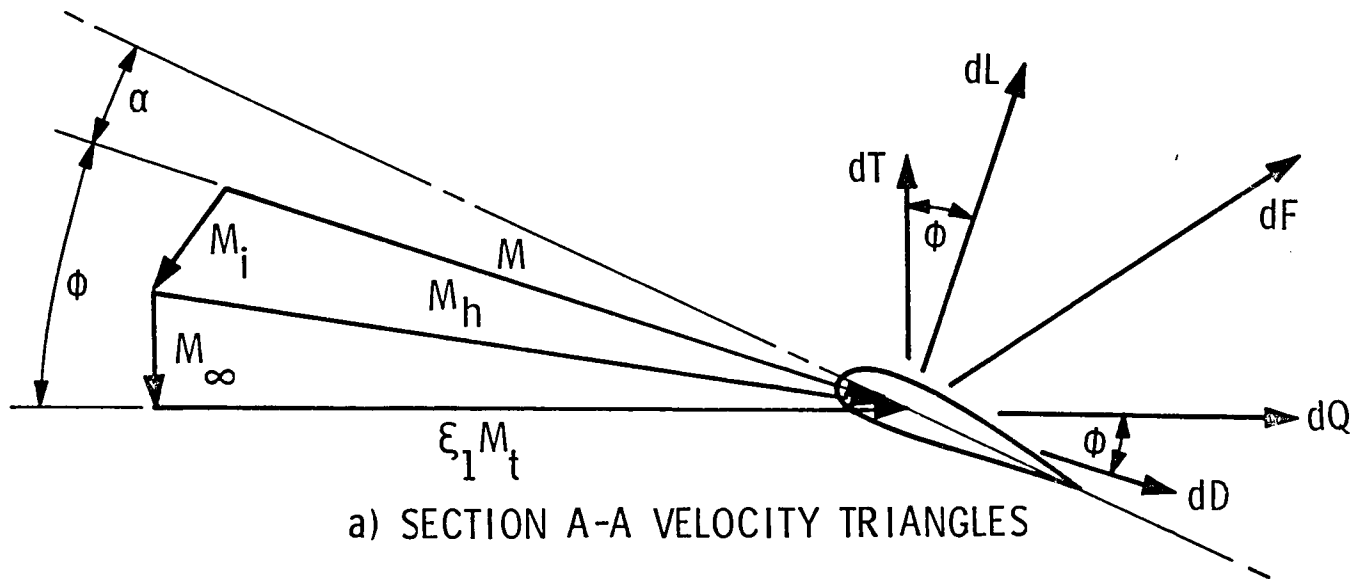
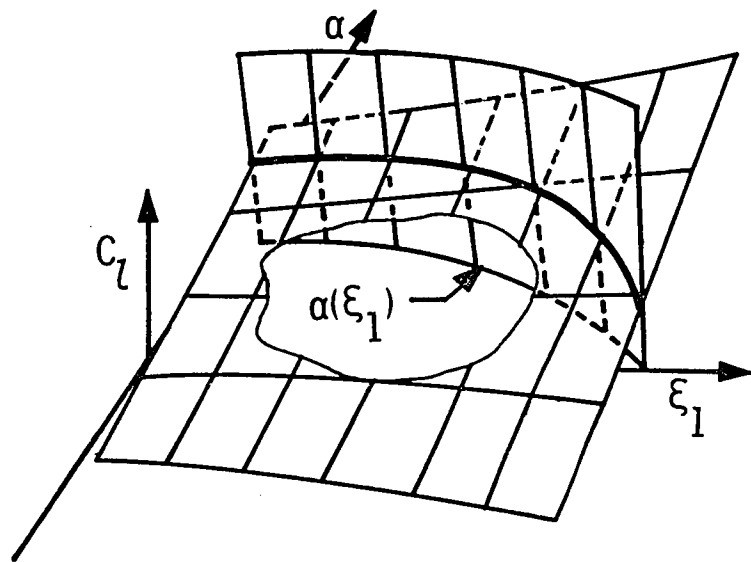
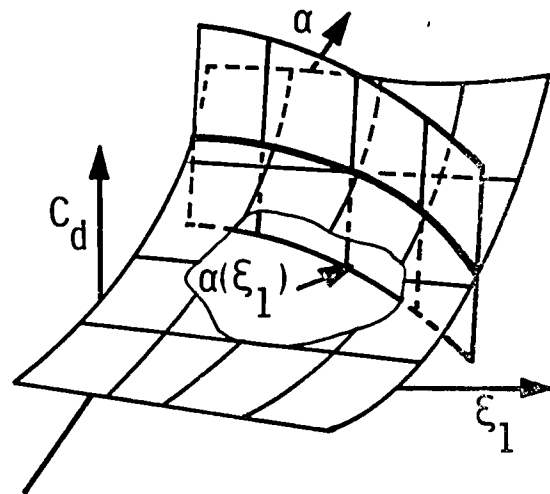


Figure 9.- Local Mach vectors and forces for a blade section.



$$\tilde{C}_l(\xi) = C_l [\xi_1, \alpha(\xi_1)]$$

a) LIFT



$$\tilde{C}_d(\xi_1) = C_d [\xi_1, \alpha(\xi_1)]$$

b) DRAG LOADING

Figure 10.- Blade lift and drag loading function.

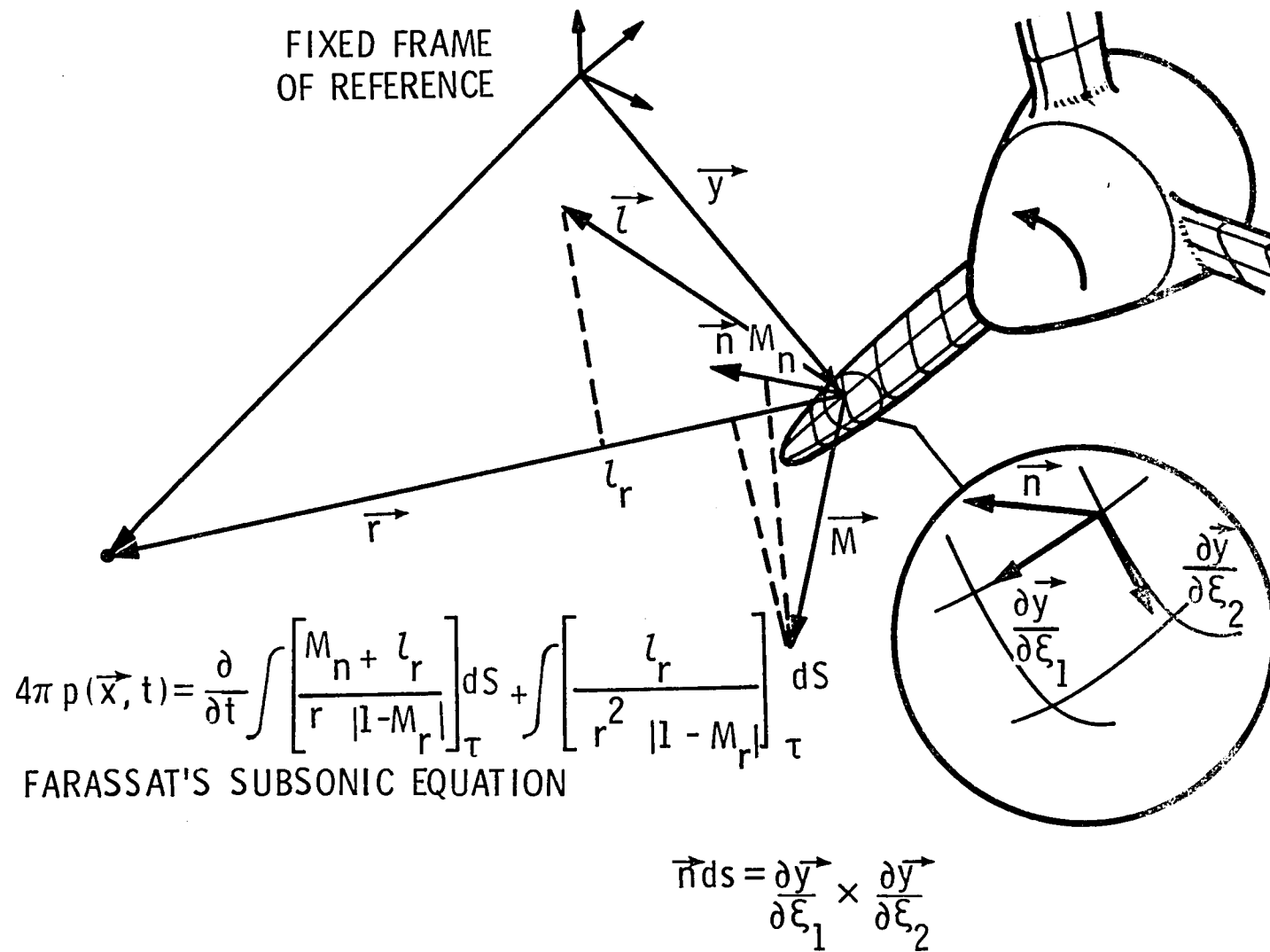


Figure 11.- Farassat's method for predicting discrete subsonic propeller noise.

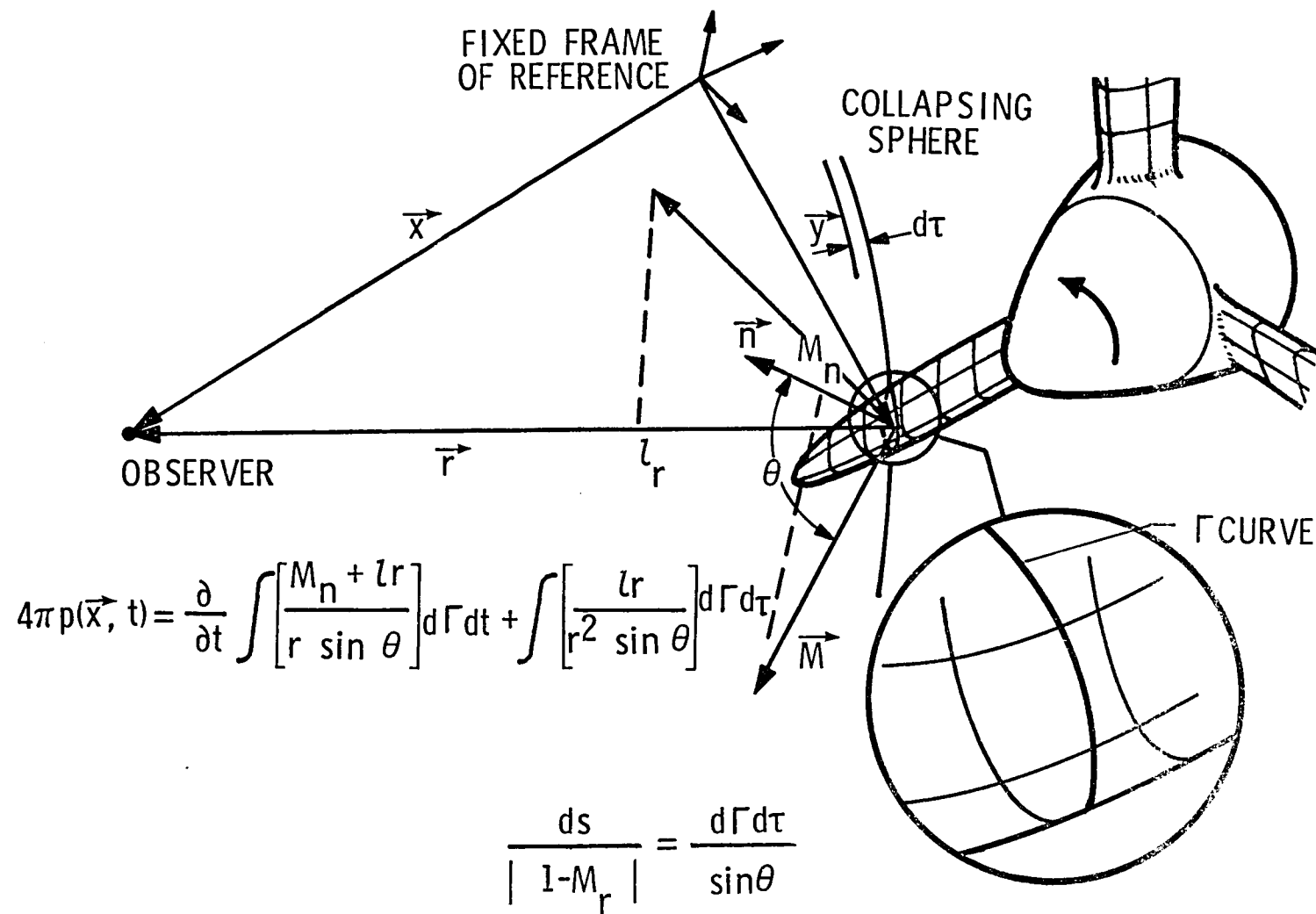
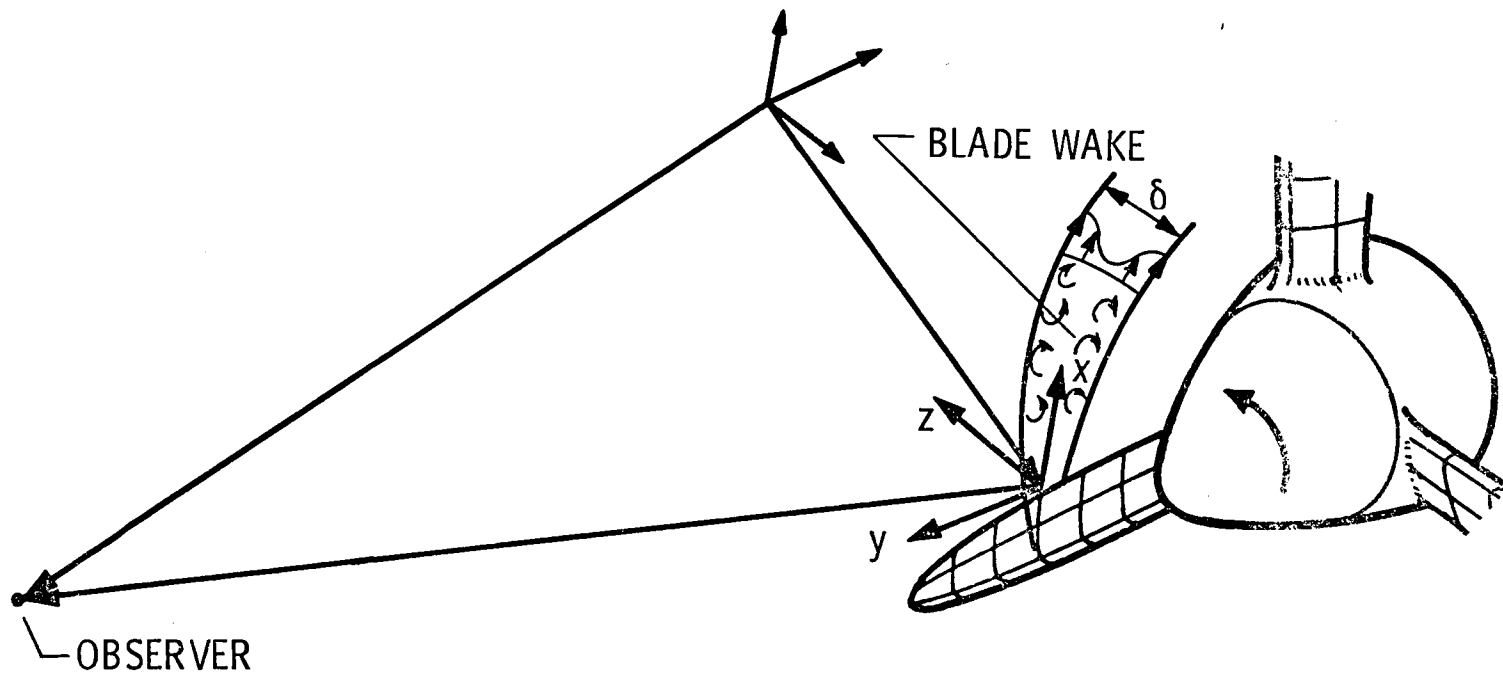


Figure 12.- Farassat's method for predicting discrete transonic propeller noise.



$$\langle p^2(\vec{x}, \omega, t) \rangle = \int_{\text{TRAILING EDGE}} \left[\frac{1}{4} \left(\frac{k_x M Z C}{2\pi \sigma^2} \right) |L^2| \tau_y(\omega) S(\omega) \right] ds$$

Figure 13.- Schlinker and Amiet's method for predicting trailing edge broadband noise.

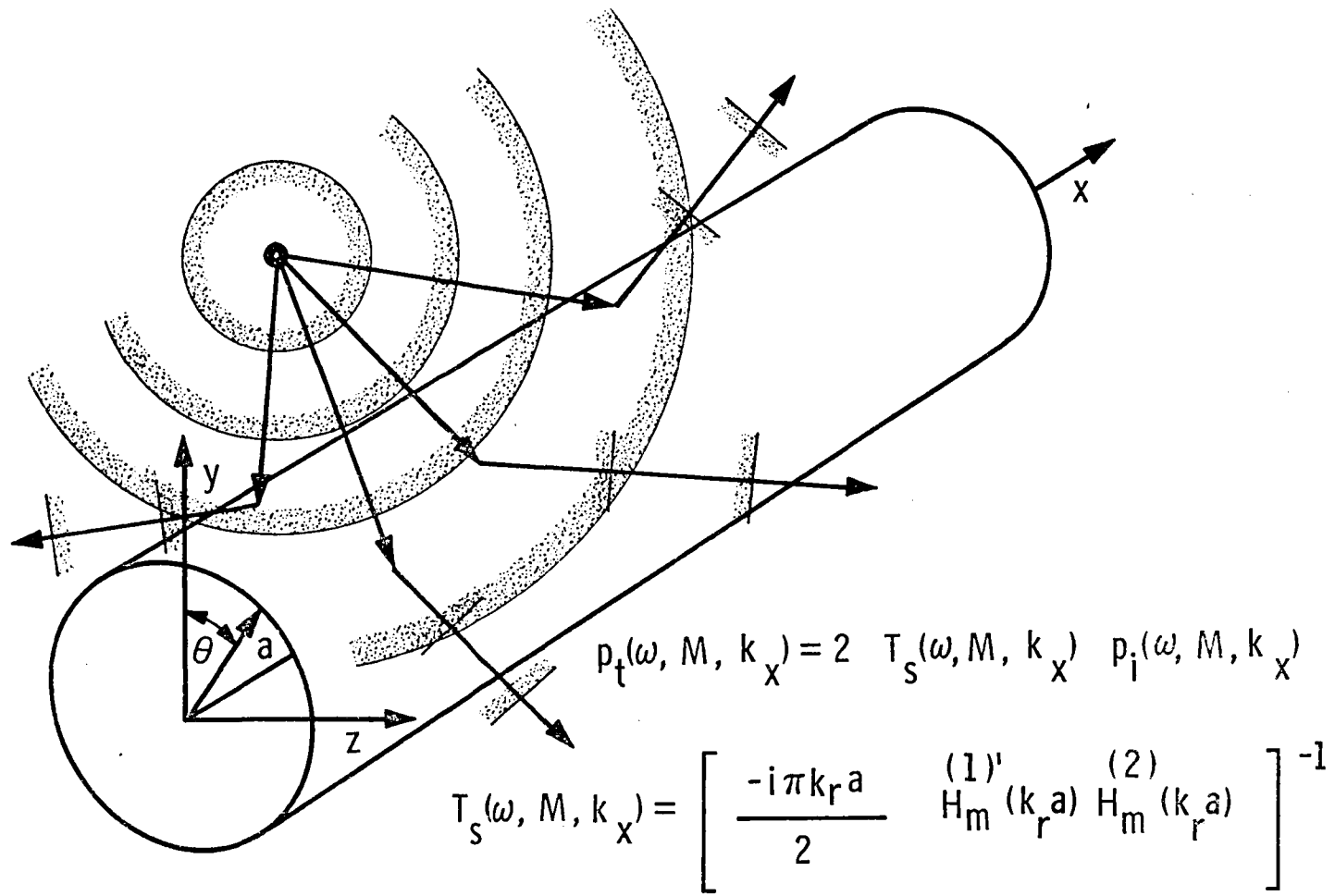


Figure 14.- Scattering of nearfield source noise by a cylindrical fuselage.

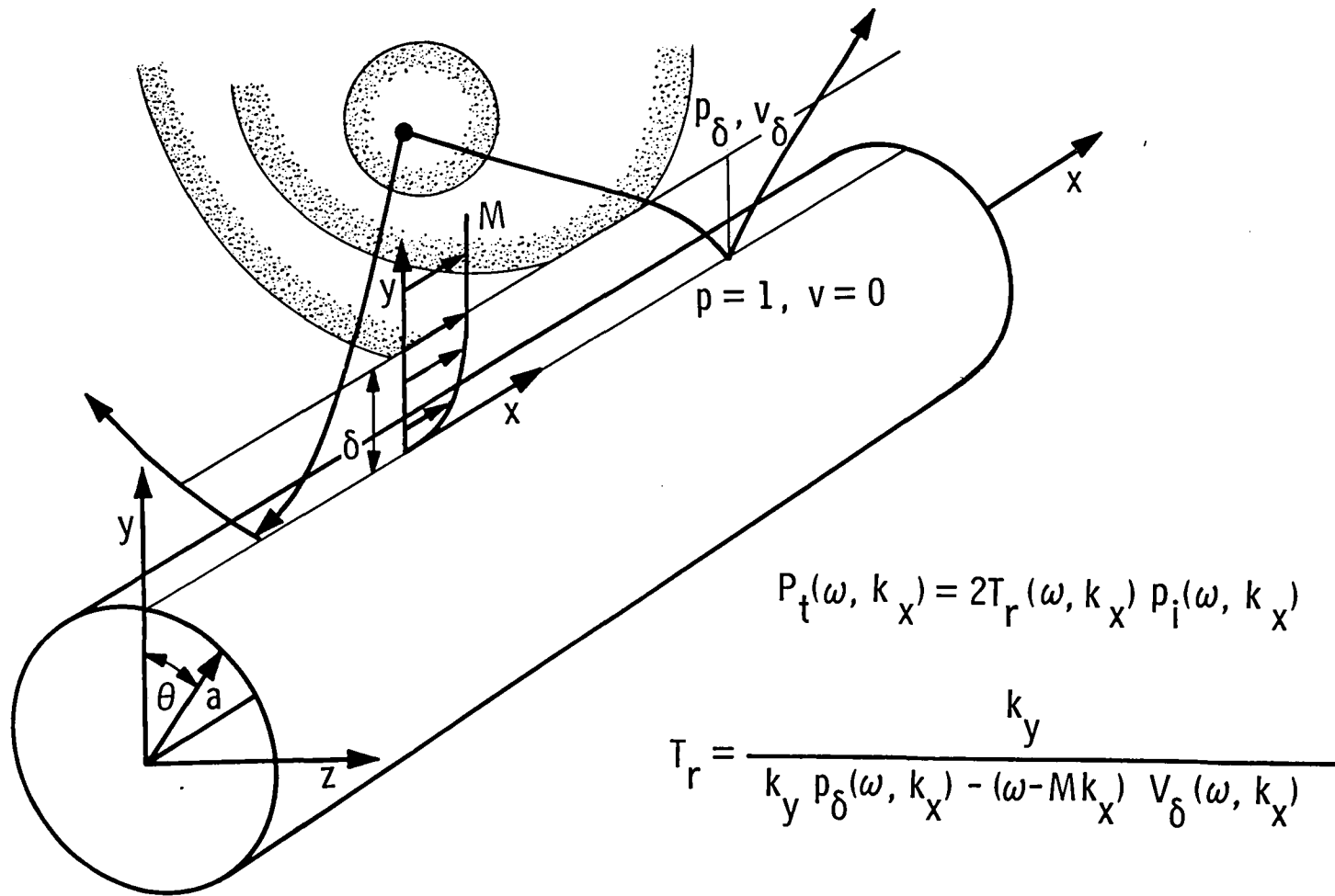


Figure 15.- Fuselage boundary layer refraction of nearfield source noise.

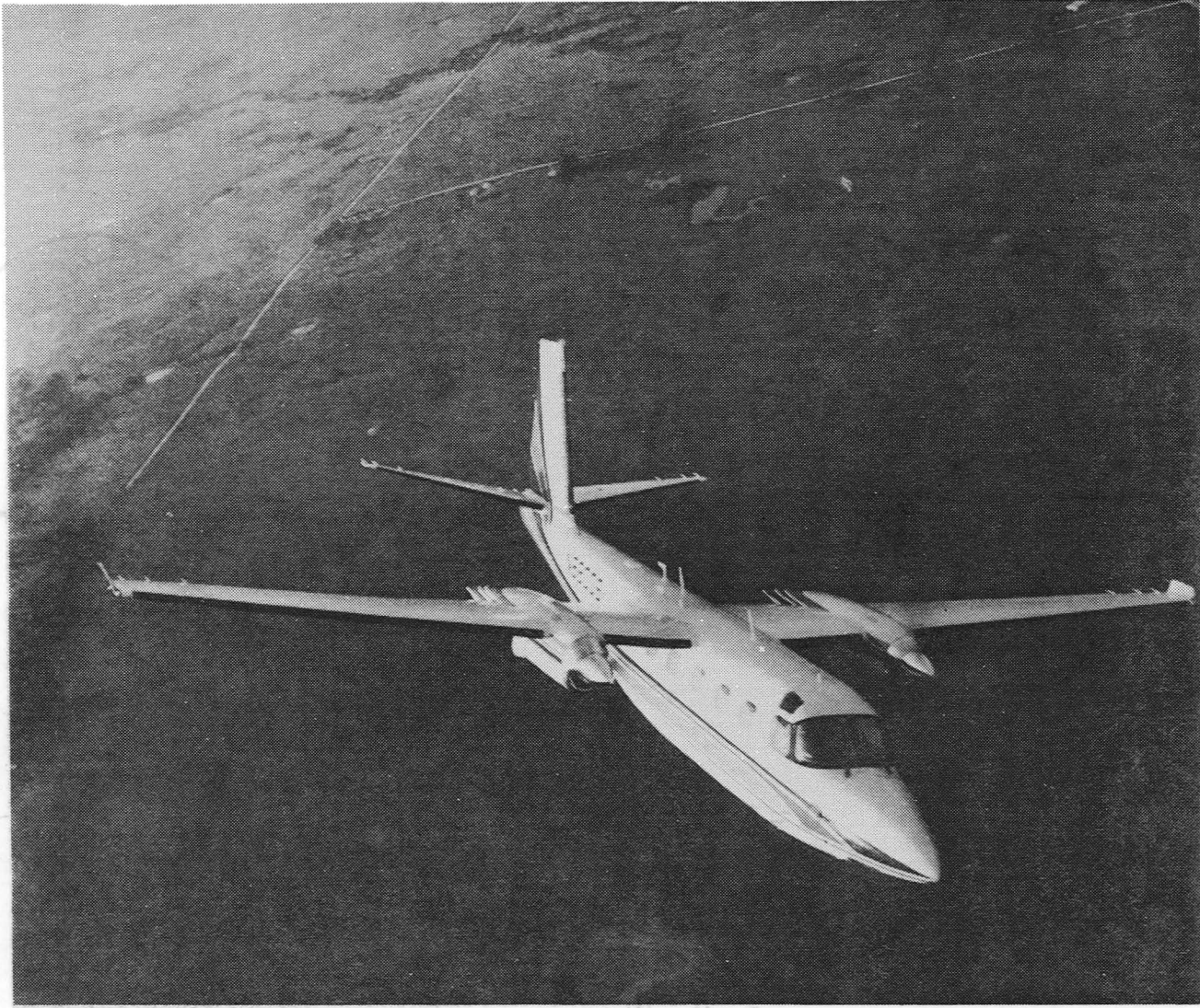
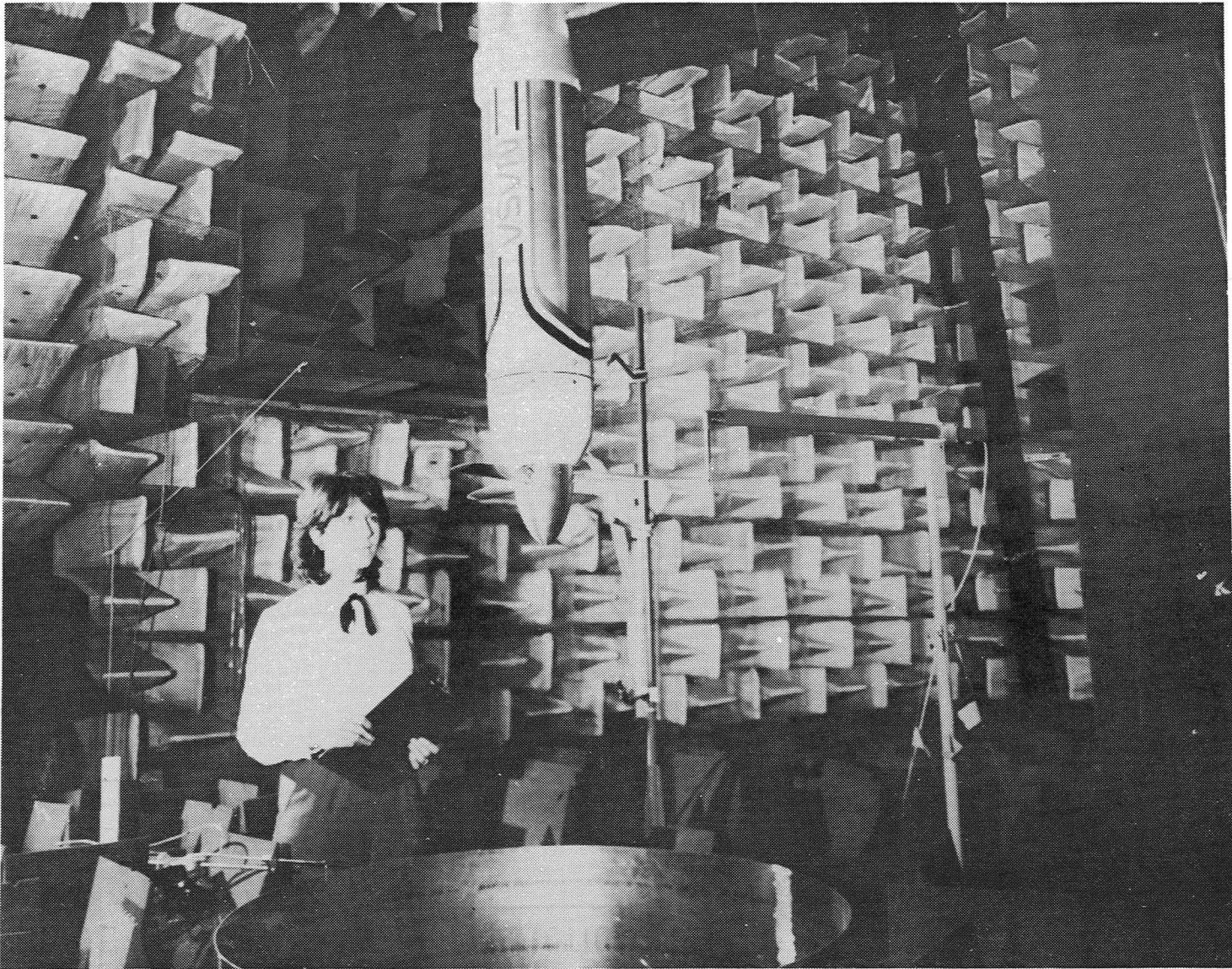


Figure 16.- Twin subsonic propeller aircraft in flight.



30 Figure 17. Quarter-scale subsonic propeller in test chamber.

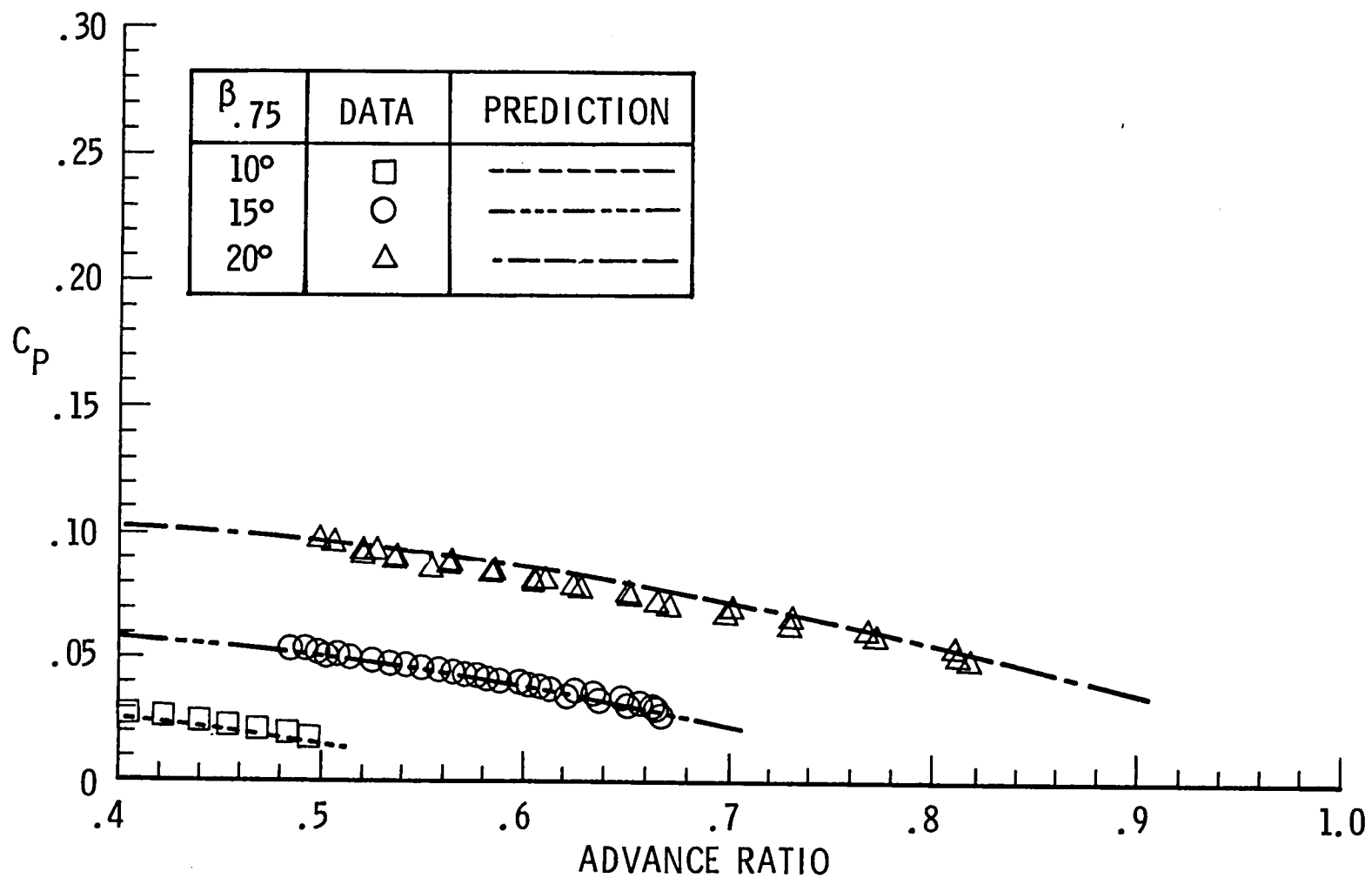


Figure 18.- Power coefficient of 1/4-scale subsonic propeller.

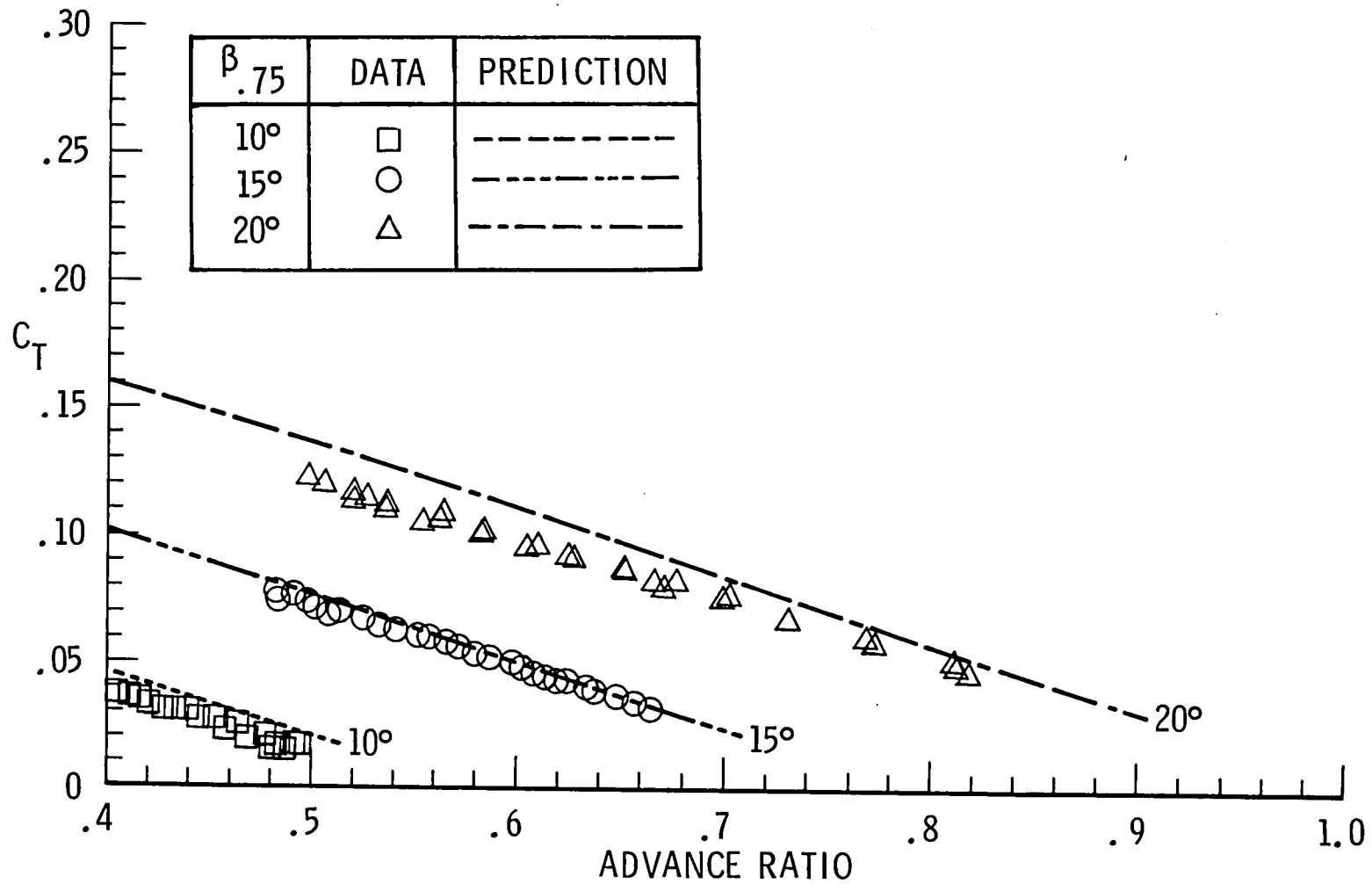


Figure 19.- Thrust coefficient of 1/4-scale subsonic propeller.

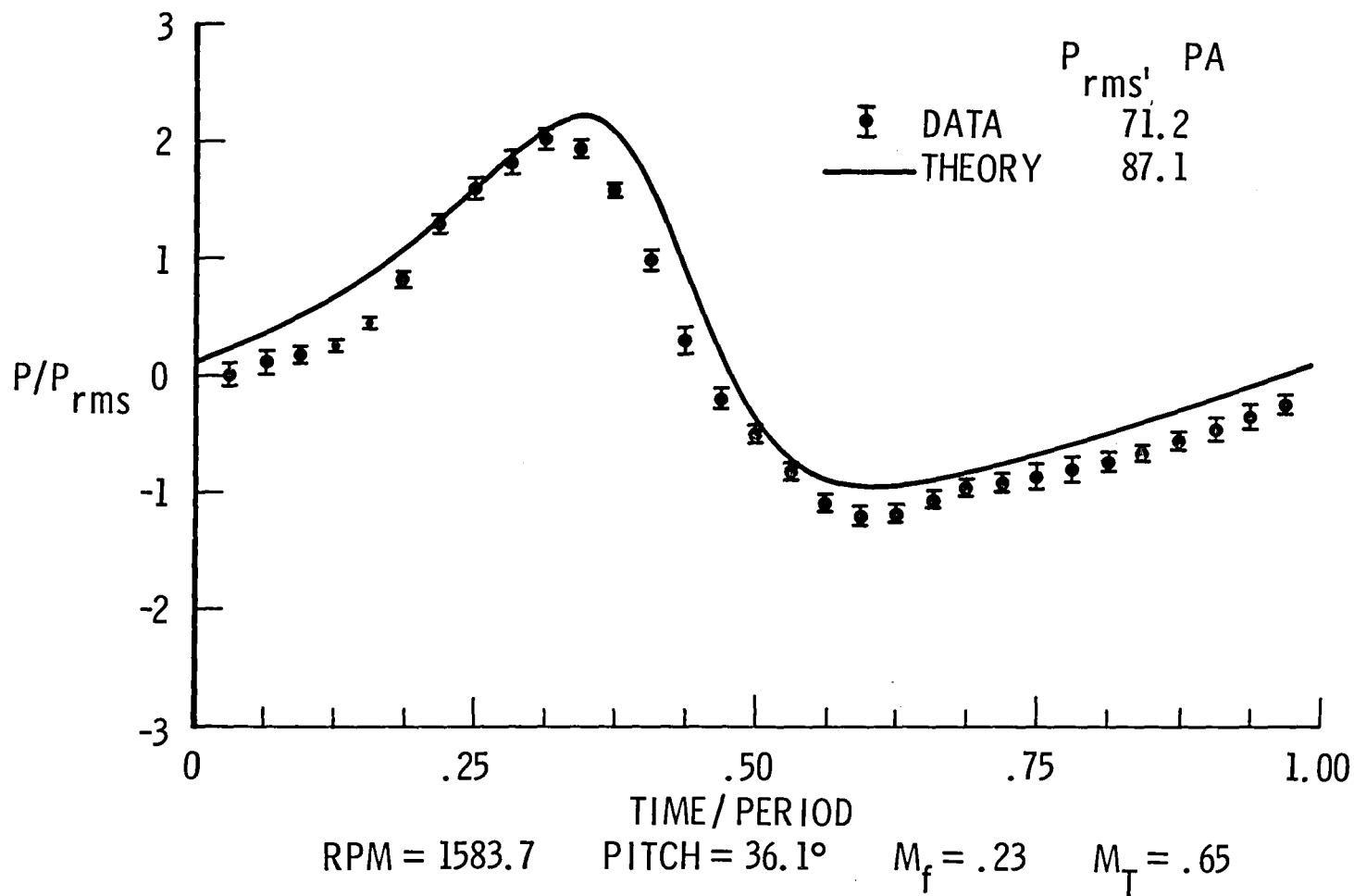


Figure 20.- Inflight nearfield subsonic propeller noise signal.

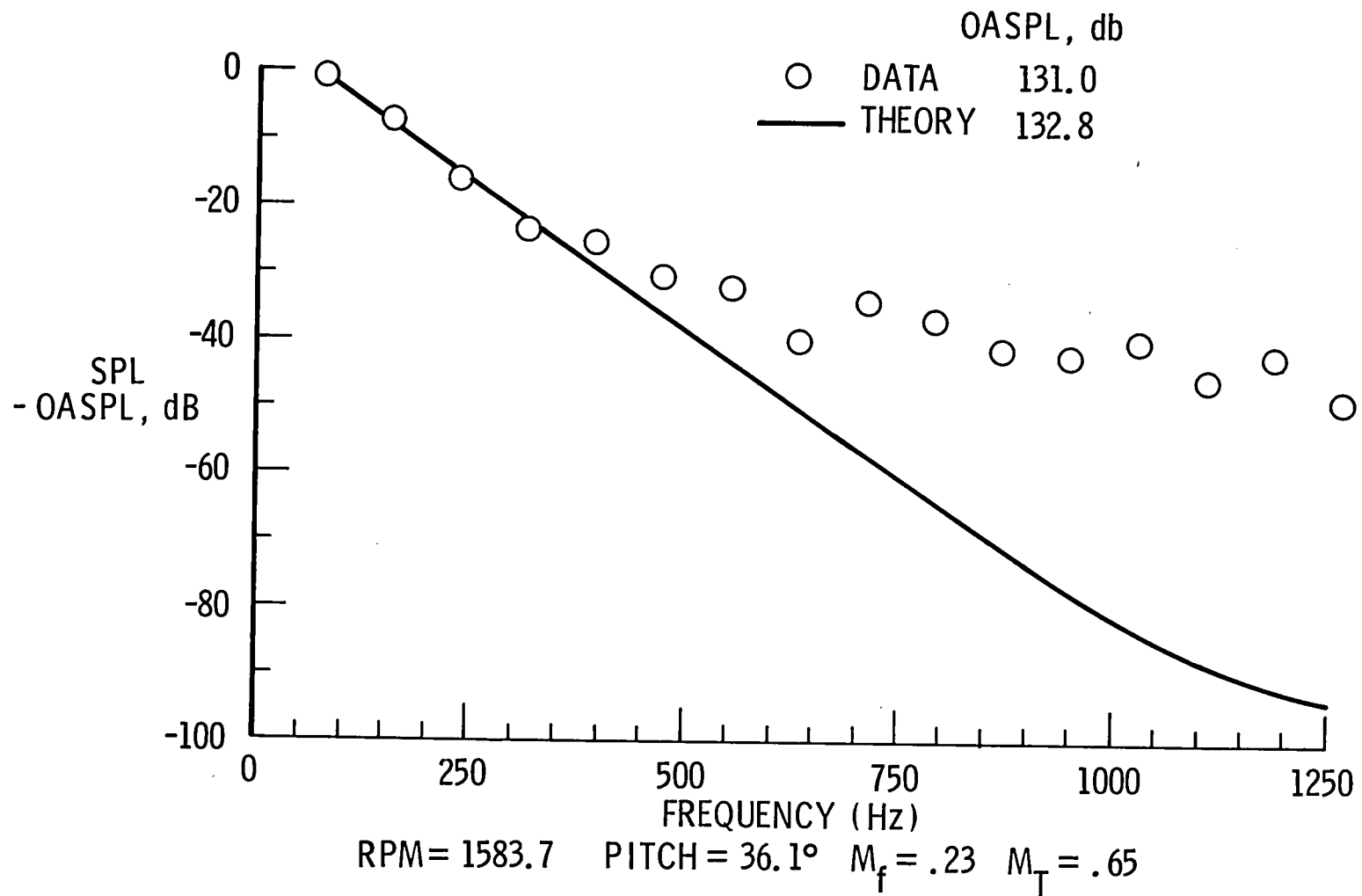


Figure 21.- Inflight nearfield subsonic propeller noise spectrum.

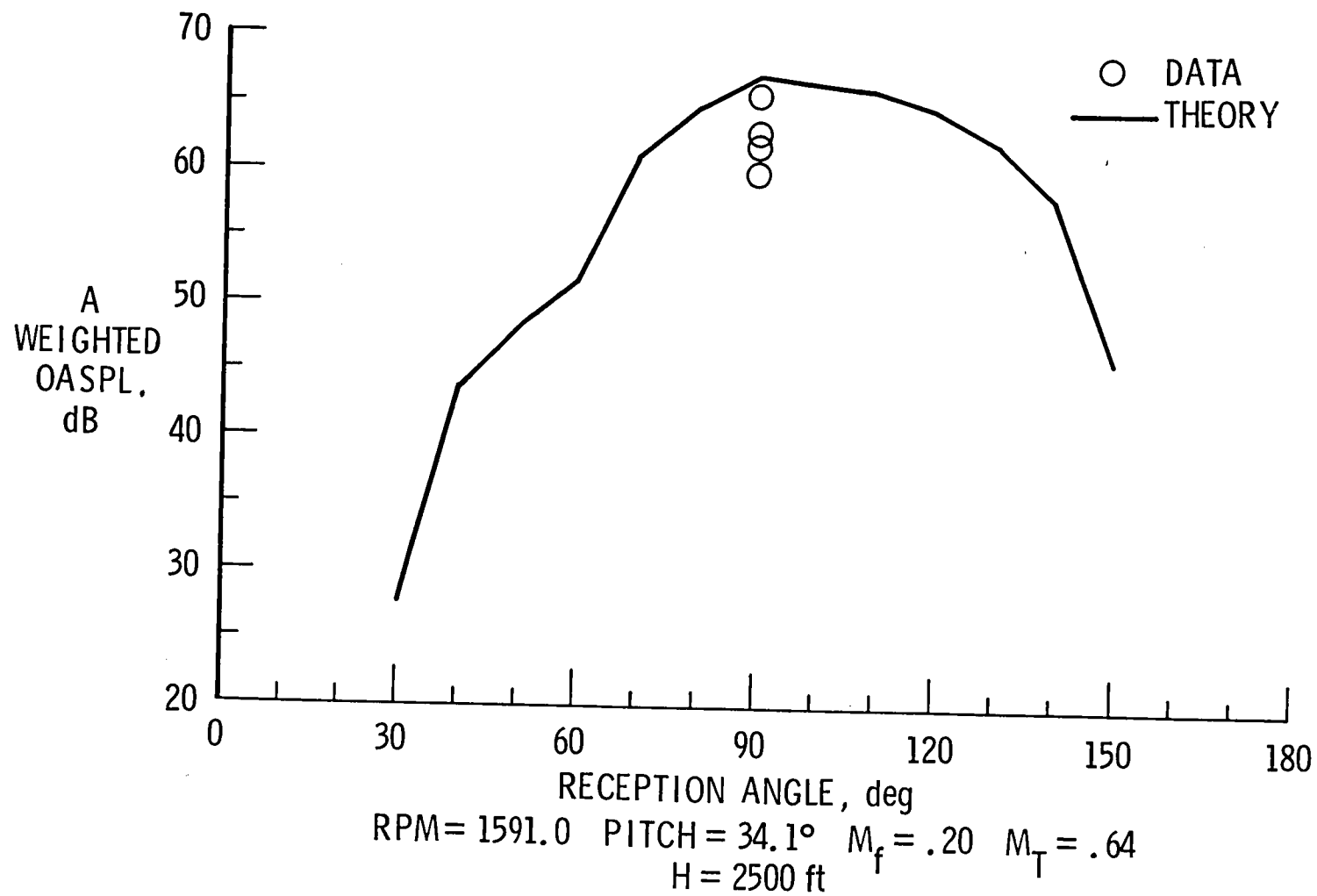


Figure 22.- Twin subsonic propeller aircraft flyover noise levels.

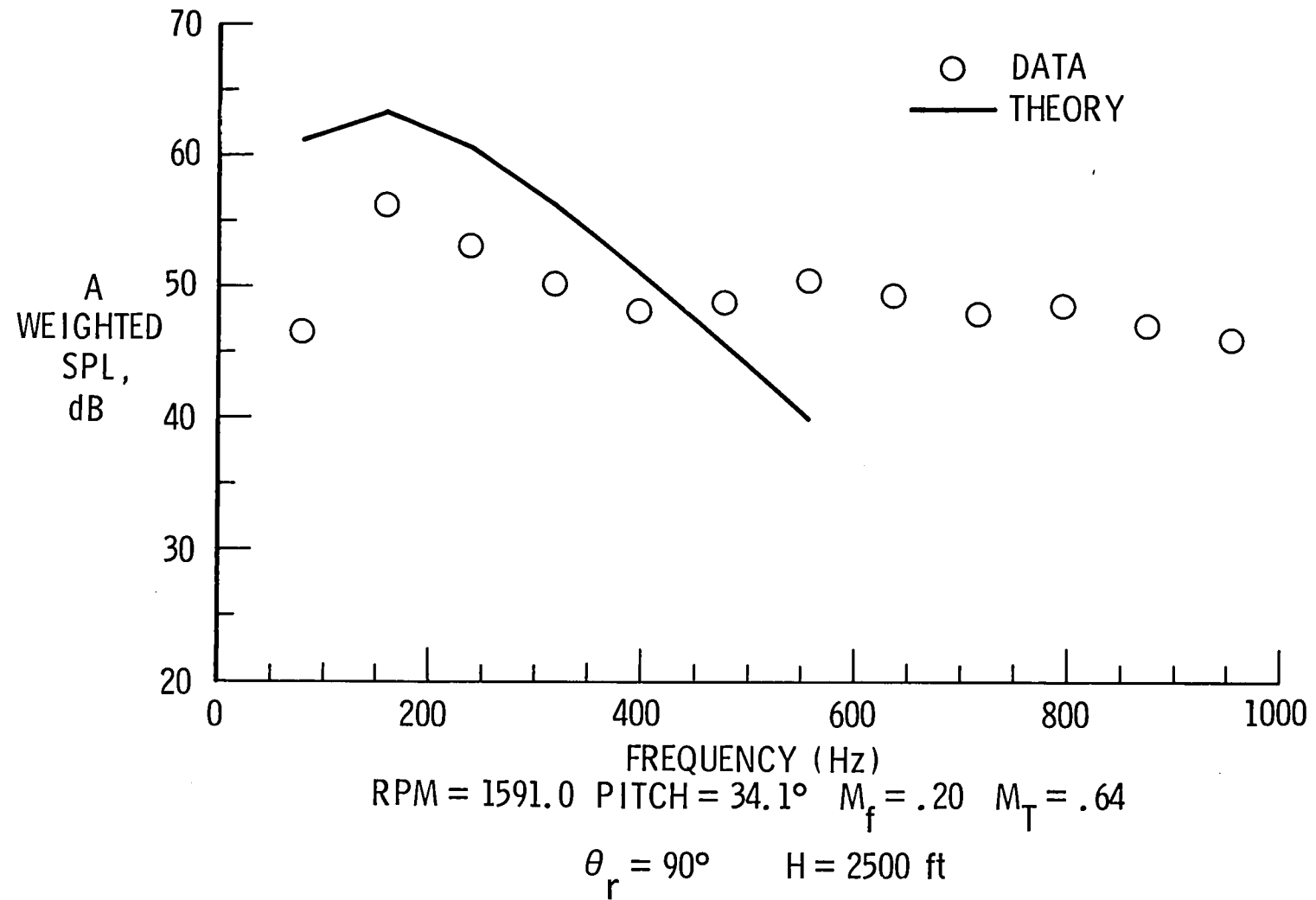


Figure 23.- Twin subsonic propeller aircraft flyover noise spectrum.



Figure 24.- Jetstar/Propfan flight tests.

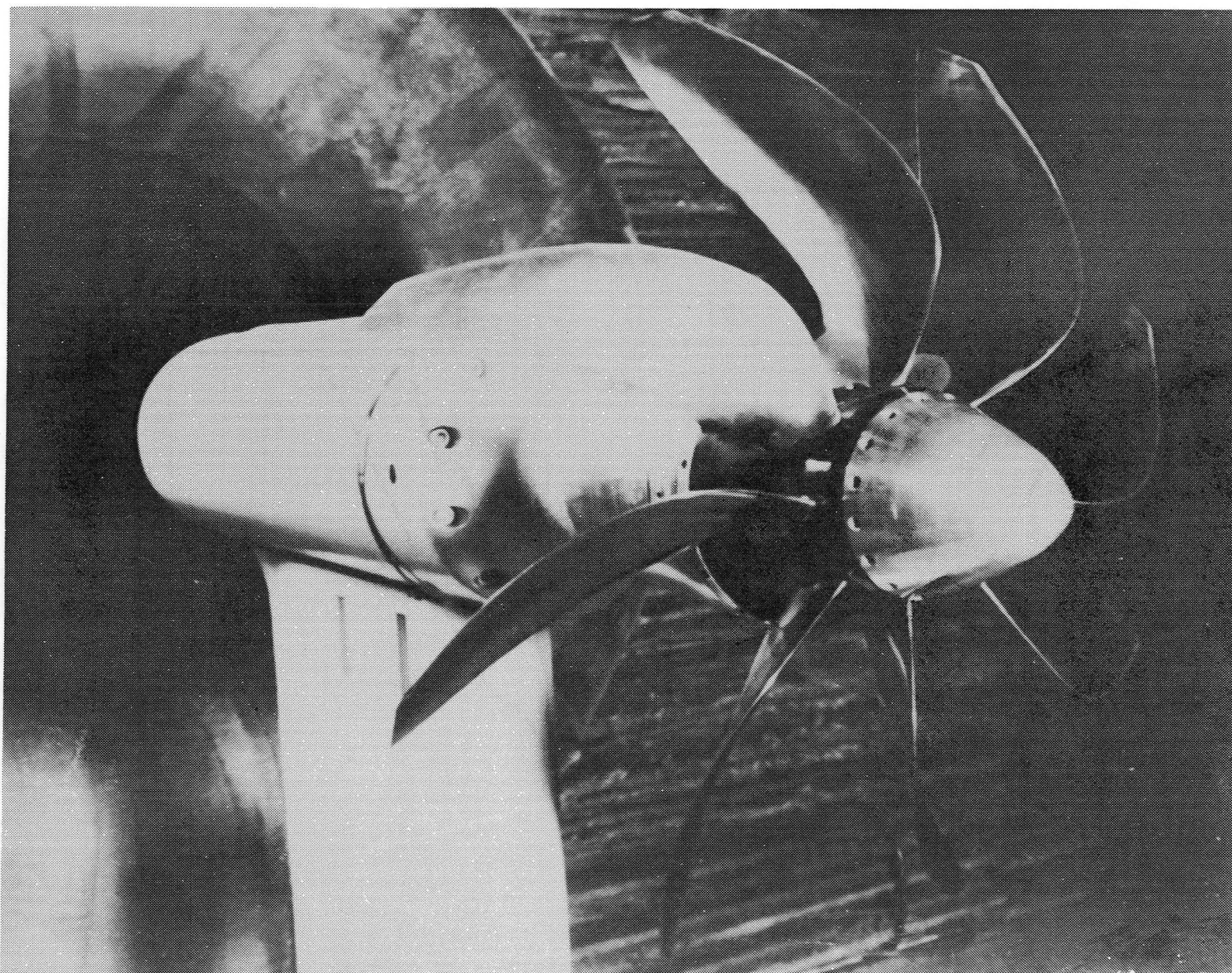


Figure 25.- Propfan performance tests.

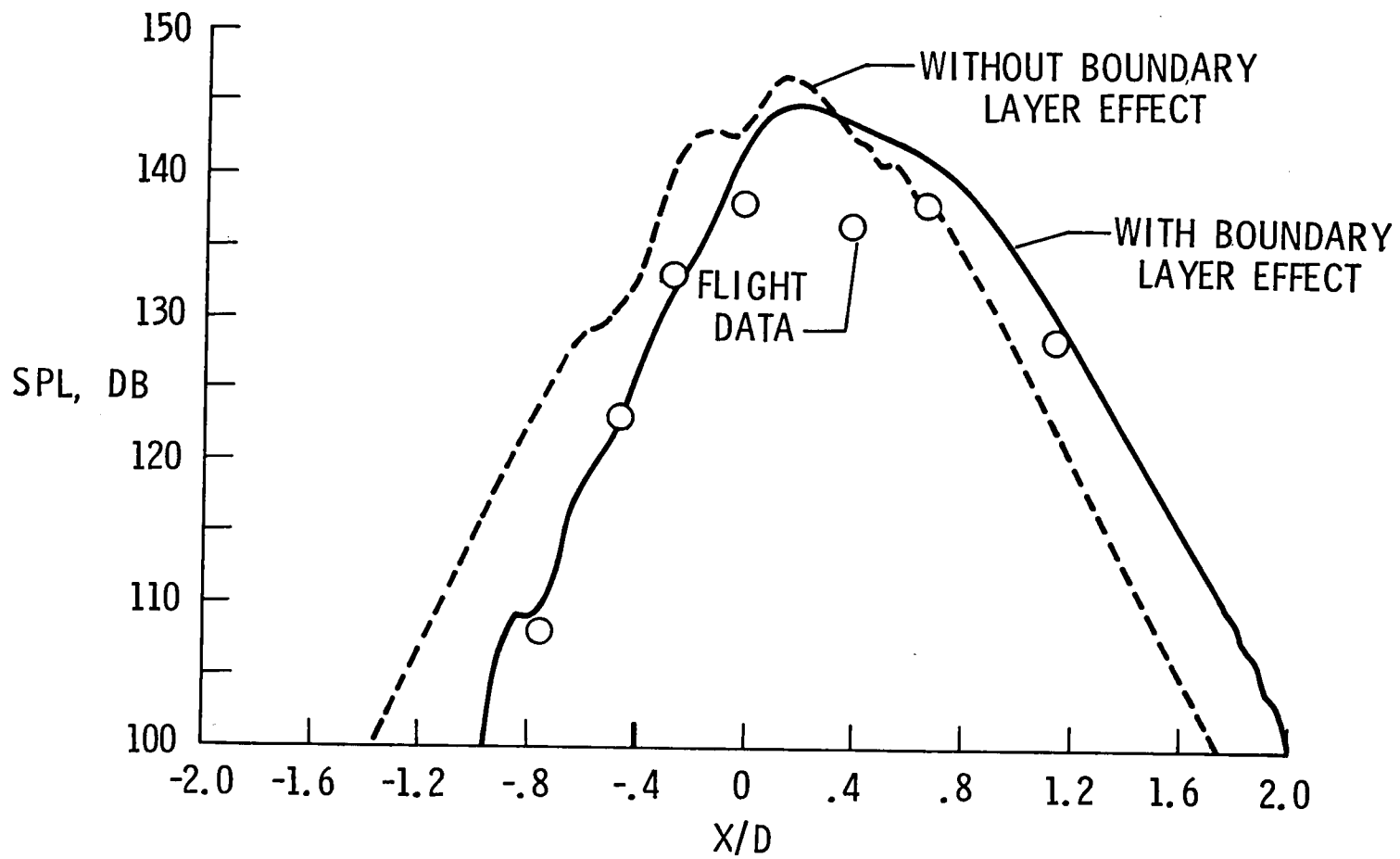


Figure 26.- Jetstar fuselage surface noise.

1. Report No. NASA TM 85636	2. Government Accession No.	3. Recipient's Catalog No.	
4. Title and Subtitle Propeller Noise Prediction		5. Report Date May 1983	
		6. Performing Organization Code 505-40-12-01	
7. Author(s) William E. Zorumski		8. Performing Organization Report No.	
		10. Work Unit No.	
9. Performing Organization Name and Address NASA Langley Research Center Hampton, VA 23665		11. Contract or Grant No.	
		13. Type of Report and Period Covered Technical Memorandum	
12. Sponsoring Agency Name and Address National Aeronautics and Space Administration Washington, DC 20546		14. Sponsoring Agency Code	
		15. Supplementary Notes Presented at Acoustical Society of America Meeting, May 10, 1983 in Cincinnati, Ohio.	
16. Abstract Analytic propeller noise prediction involves a sequence of computations culminating in the application of acoustic equations. This paper describes the prediction sequence currently used by NASA in its ANOPP (Aircraft Noise Prediction) program. No attempt is made here to review the state of the art of noise prediction. Some elements of this sequence represent classic results while others represent the most recent publications. The elements of the sequence are called program modules. The first group of modules analyzes the propeller geometry, the aerodynamics, including both potential and boundary layer flow, the propeller performance, and the surface loading distribution. This group of modules is based entirely on aerodynamic strip theory. The next group of modules deals with the actual noise prediction, based on data from the first group. Deterministic predictions of periodic thickness and loading noise are made using Farassat's time-domain methods. Broadband noise is predicted by the semi-empirical Schlinker-Amiet method. Near-field predictions of fuselage surface pressures include the effects of boundary layer refraction and (for a cylinder) scattering. Far-field predictions include atmospheric and ground effects. Comparisons are made to experimental data from subsonic and transonic propellers and NASA's future directions in propeller noise technology development are indicated.			
17. Key Words (Suggested by Author(s)) Propeller performance Propeller noise Noise prediction		18. Distribution Statement Unclassified - Unlimited Subject Category 71	
19. Security Classif. (of this report) Unclassified	20. Security Classif. (of this page) Unclassified	21. No. of Pages 61	22. Price* A04



100

100

LANGLEY RESEARCH CENTER



3 1176 01323 7996



7